The Astrophysical Journal, 764:119 (18pp), 2013 February 20 doi:10.1088/0004-637X/764/2/119

GAMMA-RAY OBSERVATIONAL PROPERTIES OF TeV-DETECTED BLAZARS

G. D. Şentürk[1], M. Errando[2,3], M. Böttcher[4,5], and R. Mukherjee[2]
[1] Physics Department, Columbia University, 550 West 120th Street, New York, NY 10027, USA; gds2110@columbia.edu
[2] Department of Physics & Astronomy, Barnard College, Columbia University, 3009 Broadway, New York, NY 10027, USA
[3] Columbia Astrophysics Laboratory, Columbia University, 550 West 120th Street, New York, NY 10027, USA
[4] Astrophysical Institute, Department of Physics and Astronomy, Ohio University, Athens, OH, USA
[5] Centre for Space Research, North-West University Potchefstroom, Potchefstroom 2531, South Africa
Received 2012 September 9; accepted 2012 December 18; published 2013 January 30

ABSTRACT

The synergy between the *Fermi*-LAT and ground-based Cherenkov telescope arrays gives us the opportunity for the first time to characterize the high-energy emission from blazars over 5 decades in energy, from 100 MeV to 10 TeV. In this study, we perform a *Fermi*-LAT spectral analysis for TeV-detected blazars and combine it with archival TeV data. We examine the observational properties in the γ-ray band of our sample of TeV-detected blazars and compare the results with X-ray and GeV-selected populations. The spectral energy distributions (SEDs) that result from combining *Fermi*-LAT and ground-based spectra are studied in detail. Simple parameterizations such as a power-law function do not always reproduce the high-energy SEDs, where spectral features that could indicate intrinsic absorption are observed.

Key words: galaxies: active – galaxies: nuclei – gamma rays: general

Online-only material: color figures

1. INTRODUCTION

Active galactic nuclei (AGNs) are extreme objects with observed luminosity outshining their host galaxy. These sources are believed to be powered by accretion onto a central supermassive black hole, commonly display relativistic jets, and exhibit non-thermal continuum emission extending from the radio band to X- and γ-rays. Blazars constitute a subclass of AGNs, with jet axes oriented close to the observer's line of sight. Relativistic beaming gives rise to distinctive observational features in blazars, such as strongly anisotropic radiation, superluminal motion, high polarization, and rapid variability (Urry & Padovani 1995). Blazars are divided into two subclasses, flat spectrum radio quasars (FSRQs) and BL Lacertae objects (BL Lacs). FSRQs are observationally characterized by broad spectral lines in the optical band, which are weak or not present in BL Lacs. The spectral energy distribution (SED) of blazars exhibits a two-component structure, with a low-energy component peaking between infrared (IR) and X-ray energies, and a high-energy one between X- and γ-rays. The low-energy component is believed to be dominated by synchrotron emission from relativistic electrons in the jet (Kembhavi & Narlikar 1999). The peak frequency of the synchrotron component of the SED ($\nu_{\rm syn}$) is used to subclassify BL Lacs into low (LBLs; $\nu_{\rm syn} < 10^{14}$ Hz), intermediate (IBL; $\nu_{\rm syn} \sim 10^{14}$–$10^{15}$ Hz), and high-frequency-peaked BL Lacs (HBL; $\nu_{\rm syn} > 10^{15}$ Hz).

The high-energy component of the blazar SED has been historically less studied, due to the later development of hard X-ray and γ-ray detectors compared to those of longer frequency bands. The synchrotron self-Compton (SSC) model is the simplest scenario that explains the high-energy emission of blazars, by inverse-Compton (IC) upscattering of soft synchrotron photons off the same electrons that have undergone synchrotron cooling (Maraschi et al. 1992). Throughout the text, we refer to the high-energy component of the blazar SED as "IC component." An additional IC target photon field external to the jet is often invoked (see, e.g., W Comae: Acciari et al. 2009d). This mechanism is referred to as external-Compton (EC), and several possible sources for the external photon field have been set forth (Böttcher 2010). Other models suggest a significant contribution from hadronic processes to the high-energy output (Mannheim & Biermann 1992).

A good spectral characterization of the high-energy peak of the blazar spectrum (keV–TeV band) is essential to discriminate between the aforementioned models. During the EGRET era covering 1991–2001 (Thompson et al. 1993), only five blazars were known at TeV energies: Mrk 421, Mrk 501, 1ES 1959+650, PKS 2155-304, and 1ES 2344+514; thanks to the first generation of ground-based Imaging Atmospheric Cherenkov Telescopes (IACTs; Whipple, Kildea et al. 2007; HEGRA, Pühlhofer et al. 2003; Durham Mark 6, Armstrong et al. 1999; and Telescope Array, Aiso et al. 1997). Only three of these sources were detected by EGRET (Mrk 501 was only marginally detected and 1ES 2344+514 was not seen at all). By the time *Fermi* started operations (2008 August), the number of known TeV blazars had increased to 21 with the second generation of IACTs in operation (VERITAS, Weekes et al. 2010; MAGIC, Aleksić et al. 2012; HESS, Bernlöhr et al. 2003). This number has doubled since then, with most TeV blazars also being detected in the GeV range by *Fermi*-LAT.

For the first time now, good quality spectra are available both from *Fermi*-LAT in the high-energy (HE; 0.1 GeV $< E <$ 100 GeV) γ-ray band and IACTs in the very high energy (VHE; $E >$ 100 GeV) γ-ray band for more than two dozen sources. The combined spectral data cover up to five decades in energy, giving a detailed description of the high-energy peak of the blazar SED. Recent studies have explored this newly available data sample, focusing on the GeV properties of TeV-selected blazars (Abdo et al. 2009), or deriving jet parameters assuming leptonic emission models (Zhang et al. 2012). These studies are similar to earlier studies carried out on a limited sample of TeV-detected blazars (e.g., Wagner 2008).

In this paper we study the GeV–TeV observational properties of the high-energy emission in blazars that are detected in the TeV band. Section 2 describes the population of TeV blazars,

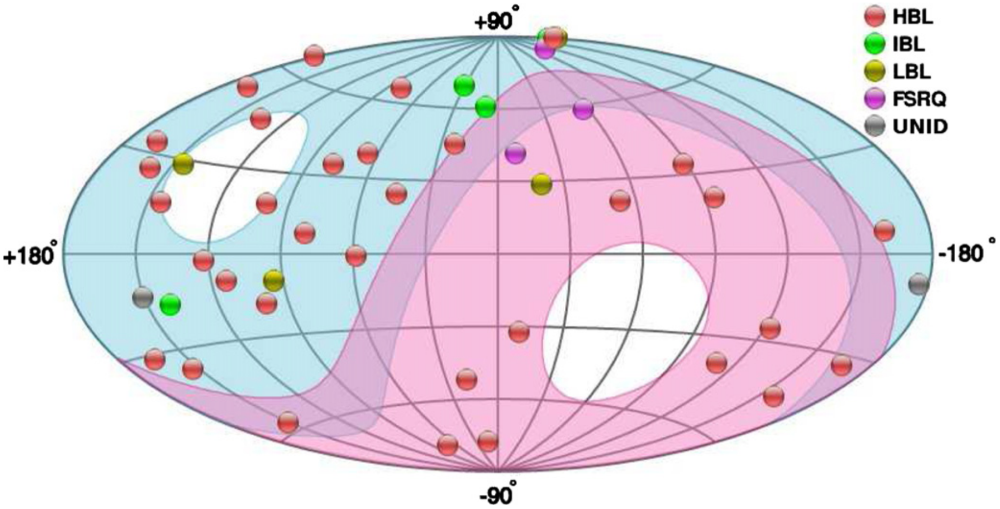

Figure 1. Sky map of TeV blazars in galactic coordinates, as of 2012 January, generated using TeVCat (http://tevcat.uchicago.edu/). The blue and pink shaded areas represent VERITAS/MAGIC and HESS visibilities, respectively. A total of 46 sources consisting of 33 HBLs, 4 IBLs, 4 LBLs, 3 FSRQs, and 2 sources that were formerly classified as AGNs of unknown type (UNID), namely IC 310 and VER J0521+211, are shown. VER J0521+211 is now identified as a BL Lac (Errando et al. 2011b) and recent studies suggest that the high-energy radiation from IC 310 originates from a blazar-like emission mechanism (Kadler et al. 2012).

(A color version of this figure is available in the online journal.)

giving census information, investigating luminosity, redshift, and photon index distributions among different blazar types. In Section 3, we study TeV blazars that appear in the *Fermi* data and outline their GeV properties with respect to the rest of the *Fermi* blazars. Section 4 defines our sample and focuses on general observational TeV properties of our objects. In Section 5, we give a detailed description of the *Fermi* analysis that we performed on our TeV blazar sample. Finally, Section 6 discusses various observational characteristics of the studied sources based on their GeV–TeV spectral shapes, such as the peak frequency of the IC component, absorption-like spectral features, and variability. Throughout the text, the symbol σ is used to designate the standard deviation, as a measure of statistical significance.

2. TeV BLAZARS

Mkn 421 was the first blazar and extragalactic object to be discovered as a VHE γ-ray emitter, detected with the Whipple telescope in 1992 (Punch et al. 1992). Since then, different candidate selection methods have been applied to radio, X-ray or HE data with the aim of finding new "TeV" blazars, i.e., detected in the VHE regime (Costamante & Ghisellini 2002; de la Calle Pérez et al. 2003; Behera & Wagner 2009), leading to the discovery of most of the known TeV blazars. To date, 44 blazars and 2 AGNs of unknown type have been detected in the VHE range,[6] with a census consisting of 33 HBLs, 4 IBLs, 4 LBLs, and 3 FSRQs (see Figure 1). In this work, we have studied the blazars that have a published TeV spectrum as of 2011 February (referred to as the "sample" in the remainder of the text).

The redshift (z) of TeV blazars in our sample ranges from 0.031 (HBL Mrk 421) to 0.536 (FSRQ 3C 279), and nearly one-fourth of the population does not have a secure redshift. This lack is due to the fact that optical emission lines are typically weak or absent in BL Lac objects, rendering direct redshift measurements difficult. The majority of known-redshift TeV blazars are located at $z < 0.2$, mostly due to the absorption from the extragalactic background light (EBL). Figure 2 illustrates the redshift distribution of all TeV blazars. The TeV FSRQs are the most distant objects in the population with redshift ranging from 0.36 to 0.536. Using archival data, we calculated the apparent isotropic luminosity of the blazars in our sample (see Section 4)

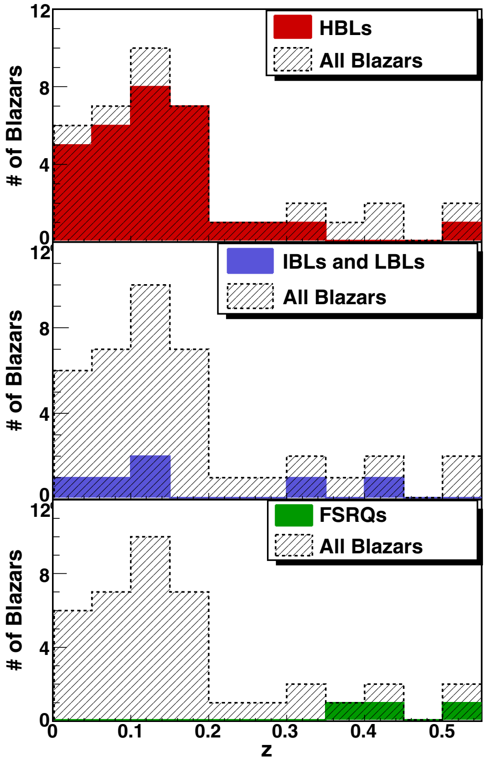

Figure 2. Redshift (z) distribution of all TeV blazars as of 2012 January. The top, middle, and bottom panels also show HBLs, IBLs and LBLs, and FSRQs, respectively. Most of the blazars with known redshifts (30 out of 39) are located at $z < 0.2$. FSRQs are the most distant objects in the population. The farthest object is the FSRQ 3C 279, with a redshift of 0.536. The rest of the population does not have a secure redshift.

(A color version of this figure is available in the online journal.)

---

[6] http://tevcat.uchicago.edu/

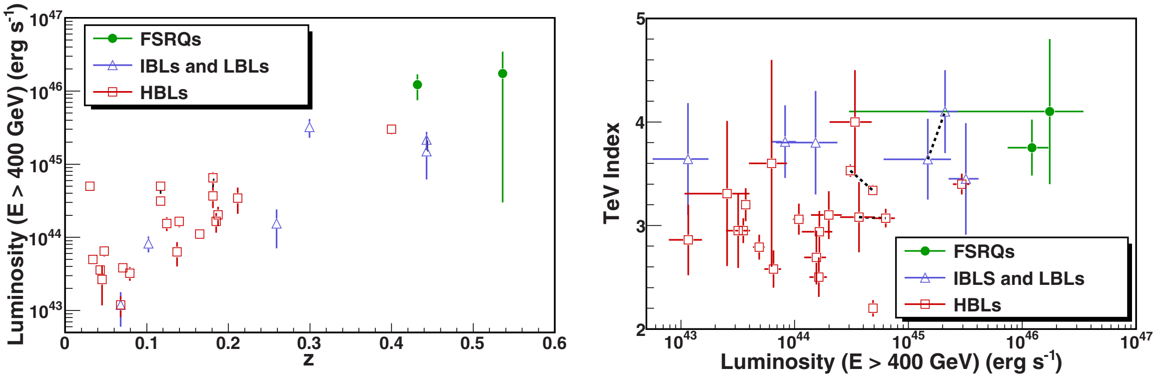

Figure 3. Left: apparent luminosity (not EBL-corrected) vs. redshift plot of TeV blazars. As expected, high-redshift objects are less likely to be seen, and in fact most of them were detected in flare states. Right: TeV index vs. apparent luminosity distribution of the same sample. For fluxes up to $\sim 10^{45}$ erg s^{-1}, the TeV index distribution is fairly homogenous. At higher luminosities, mostly soft spectrum sources are detected. FSRQs are the most luminous TeV emitters but one should note that their data come from flares only. Squares represent HBLs, triangles IBLs and LBLs, and circles FSRQs. The points representing different flux states of the same source are connected with dashed black lines (right).

(A color version of this figure is available in the online journal.)

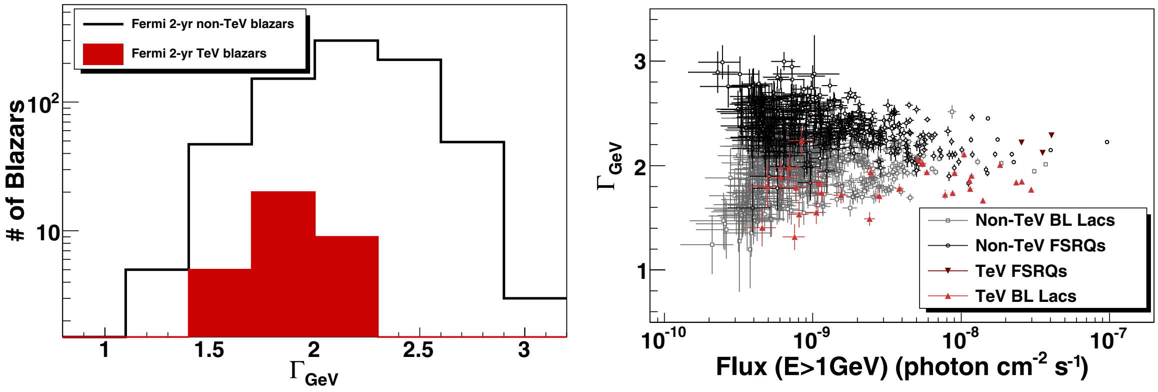

Figure 4. Left: GeV photon index (Γ_{GeV}) distribution for non-TeV blazars (black solid line) and TeV blazars (red shaded area) from the 2FGL catalog (Nolan et al. 2012). TeV emitters tend to have hard spectra in the GeV band. Right: Γ_{GeV} vs. integral flux for $E > 1$ GeV for the same sample, with gray open squares for non-TeV BL Lacs, black open circles for non-TeV FSRQs, red triangles for TeV BL Lacs and dark red inverse triangles for TeV FSRQs. TeV emitters are mostly located along the bottom of the distribution. TeV FSRQs are at the edge of the group where the luminosity is relatively higher and the index softer.

(A color version of this figure is available in the online journal.)

for $E > 400$ GeV, with the following formula:

$$L = F \times 4\pi D_L^2/(1+z)^{2-\Gamma}, \quad (1)$$

where F is the energy flux for energies above $E > 400$ GeV, D_L is the luminosity distance with Hubble constant $H_o = 71$ km s^{-1} Mpc^{-1} and the cosmological constant $\Omega_\lambda = 0.730$, z is the redshift, and Γ is the observed photon index for each blazar. Figure 3 (left) shows the luminosity versus redshift correlation for the sample. Sources at high redshifts tend to be scarce and much more luminous. The reason why we see only luminous sources at high redshifts is that the less luminous ones are too weak to be detected. On the other hand, the reason why we do not detect them in low redshifts is that we integrate over a much smaller volume and thus are less likely to see high-luminosity sources that should be scarce compared to low-luminosity ones. Note that if the luminosity is corrected for EBL absorption, which is stronger at TeV energies and high redshifts, the correlation will be steeper. Figure 3 (right) shows the TeV photon index versus luminosity correlation of the same sample. For luminosities up to $\sim 10^{45}$ erg s^{-1}, the photon index distribution is fairly homogenous.

3. *Fermi* TeV BLAZARS

The second *Fermi*-LAT catalog (2FGL) contains 1873 sources, among which 1062 are AGNs, with 435 BL Lacs, 370 FSRQs, and 257 AGNs of unknown class (Nolan et al. 2012). Thirty-six of these AGNs are TeV emitters. Figure 4 (left) shows the distribution of *Fermi* spectral indices (Γ_{GeV}) for TeV and non-TeV blazars in the 2FGL catalog. TeV-detected blazars tend to have harder GeV indices. As can be seen from Figure 4 (right), another distinguishing parameter for TeV emitters within the *Fermi* blazar population is the integral flux for energies above 1 GeV. It follows that an effective method for TeV-candidate selection in the HE γ-ray band is to look for bright hard spectrum sources and select the candidates based on their extrapolated fluxes at VHE energies. For all TeV blazars, $\Gamma_{\mathrm{GeV}} < 2.3$ and for most of them $\Gamma_{\mathrm{GeV}} < 2$, in agreement with an inverse-Compton peak frequency (ν_{IC}) located in the high-energy tail of the *Fermi* range or beyond. Figure 5 shows scatter plots of spectral indices of *Fermi*-bright AGNs (Abdo et al. 2010a) in radio, optical and X-ray bands, comparing TeV and non-TeV sources. The TeV and non-TeV AGNs occupy separate regions in the parameter space, consistent with the results in Abdo et al. (2010a), considering that most TeV AGNs are HBLs.

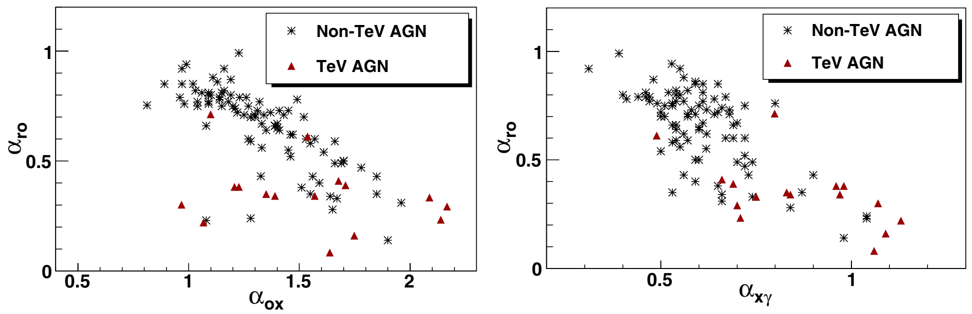

Figure 5. Scatter plots of $\alpha_{\rm ro}$ (5 GHz–5000 Å), $\alpha_{\rm ox}$ (5000 Å–1 keV) and $\alpha_{{\rm x}\gamma}$ (1 keV–100 MeV) spectral indices for the *Fermi*-LAT bright AGN sample (LBAS). Data are taken from Abdo et al. (2010a). Note the correlation between $\alpha_{\rm ro}$ and $\alpha_{{\rm x}\gamma}$. The red triangles represent TeV-detected AGNs, and asterisks non-TeV-detected ones. The TeV-emitters seem to be well isolated in $\alpha_{\rm ro}$–$\alpha_{{\rm x}\gamma}$ parameter space.

(A color version of this figure is available in the online journal.)

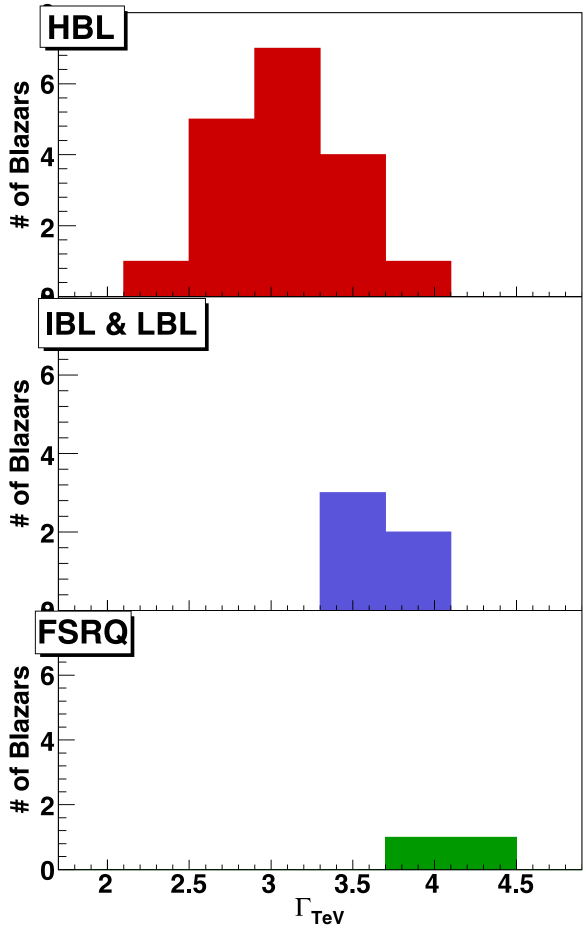

Figure 6. TeV photon index distributions for our sample (see Table 1). For blazars that have multiple published results in Table 1, the most recent one was used. Top, middle, and bottom panels show HBLs, IBLs+LBLs, and FSRQs, respectively. HBLs tend to have harder spectra than the rest of the sample. FSRQs have the softest spectra. Note that the TeV indices are not EBL-corrected.

(A color version of this figure is available in the online journal.)

4. DATA SAMPLE

Our blazar sample contains all blazars with a published VHE spectrum before 2011 February, including a total of 26 sources (see Table 1): 19 HBLs, 3 IBLs, 2 LBLs, and 2 FSRQs. TeV spectral index distributions of the whole sample are shown in Figure 6. Three of these blazars have insecure redshifts either because the spectroscopic measurements were inconclusive, or the calculations were made indirectly based on EBL absorption studies. References for the adopted redshift values in these three cases are given in Table 1. Seven of our targets were detected with EGRET and 23 of them are in the 2FGL catalog (Nolan et al. 2012). The ones that are missing in the *Fermi* data (1ES 0229+200, 1ES 0347-121, PKS 0548-322) are very hard spectrum sources that would be weak in the *Fermi* band. More than half of the sample have been detected multiple times in the VHE band. These multiple detections extending over several years and obtained mostly with different instruments suggest that spectral variability in the VHE band is a common property for VHE blazars. Even though no general pattern has been established for VHE variability, several sources have been observed to have a flux increase up to a few times their baseline emission (W Comae: Acciari et al. 2009d; Mkn 501: Albert et al. 2007e; PKS 2155-304: Aharonian et al. 2007d), occasionally accompanied by a change in spectral index (Mkn 501: Albert et al. 2007e) and minute-scale flux doubling times (Mkn 501: Albert et al. 2007e; PKS 2155-304: Aharonian et al. 2007d).

The first 27-month *Fermi* data and archival VHE spectra published before 2011 February were used to construct combined GeV–TeV SEDs in this study. Only in seven cases (RGB J0710+591, 1ES 1218+304, PKS 1222+21 (4C+21.35) PKS 1424+240, PKS 2155-304, and two different measurements for 3C 66A) were the VHE data found to overlap with the *Fermi* era. The remainder of the VHE data were taken before the *Fermi* mission.

All VHE spectra were corrected for the EBL absorption using the model by Domìnguez et al. (2011). Other background models are also available (e.g., Finke et al. 2010). However, with a different EBL model, we do not expect any significant differences in our results up to a few TeV, given the redshift and energy range of our sample. See Section 6.2 for a more detailed discussion on the EBL correction effects on our study.

5. *Fermi* ANALYSIS

The fact that most of the GeV and TeV data are not contemporaneous makes it hard to interpret the combined spectra of blazars. Moreover, *Fermi* data represent an average state over relatively long periods, whereas the VHE spectra consist of “snapshots,” mostly taken during flares. To account for blazar variability and the non-contemporaneous nature of the data set, for bright enough sources, the *Fermi* data were split into “low” and “high” flux states as described below. Thus, non-contemporaneous GeV and TeV measurements were matched in a more realistic way than directly using all the time-averaged *Fermi* data. Table 1 summarizes the *Fermi* flux states and VHE spectra used for each source.

Table 1
GeV–TeV Properties of the VHE Blazar Sample Taken from the Literature

Name	SED Type (1)	z (2)	$\log_{10}(\nu_{\rm syn}/1\,{\rm Hz})$ (3)	*Fermi* Var. (4)	*Fermi* State (5)	$\Gamma_{\rm TeV}$ (6)	I (7)	$E_{\rm th}$ (GeV) (8)	Reference (9)
RGB J0152+017	HBL	0.080	···	···	average	$2.95 \pm 0.36_{\rm stat} \pm 0.20_{\rm syst}$	2%	300	(Aharonian et al. 2008)
3C 66A*	IBL	0.444[a]	15.63	171	MAGIC	$3.64 \pm 0.39_{\rm stat} \pm 0.25_{\rm syst}$	6%	200	(Aleksić et al. 2011a)
					VERITAS	$4.1 \pm 0.4_{\rm stat} \pm 0.6_{\rm syst}$	8%	100	(Acciari et al. 2009b)
1ES 0229+200	HBL	0.140	19.45	···	average	$2.50 \pm 0.19_{\rm stat} \pm 0.10_{\rm syst}$	2%	580	(Aharonian et al. 2007b)
1ES 0347-121	HBL	0.188	17.94	···	average	$3.10 \pm 0.23_{\rm stat} \pm 0.10_{\rm syst}$	2%	250	(Aharonian et al. 2007a)
PKS 0548-322	HBL	0.069	16.84	···	average	$2.86 \pm 0.34_{\rm stat} \pm 0.10_{\rm syst}$	1%	200	(Aharonian et al. 2010)
RGB J0710+591	HBL	0.125	21.05	6	VERITAS	$2.69 \pm 0.26_{\rm stat} \pm 0.20_{\rm syst}$	3%	300	(Acciari et al. 2010c)
S5 0716+714	LBL	0.300	14.46	266	high	$3.45 \pm 0.54_{\rm stat} \pm 0.2_{\rm syst}$	9%	400	(Anderhub et al. 2009a)
1ES 0806+524	HBL	0.138	16.56	20	average	$3.6 \pm 1.0_{\rm stat} \pm 0.3_{\rm syst}$	2%	300	(Acciari et al. 2009a)
1ES 1011+496	HBL	0.212	16.74	16	high	$4.0 \pm 0.5_{\rm stat} \pm 0.2_{\rm syst}$	6%	200	(Albert et al. 2007d)
1ES 1101-232	HBL	0.186	16.88	1	average	$2.94 \pm 0.20_{\rm stat}$	3%	225	(Aharonian et al. 2007c)
Markarian 421*	HBL	0.031	18.49	44	medium	$2.20 \pm 0.08_{\rm stat} \pm 0.2_{\rm syst}$	50–200%	200	(Albert et al. 2007b)
Markarian 180	HBL	0.046	18.61	10	average	$3.3 \pm 0.7_{\rm stat} \pm 0.2_{\rm syst}$	11%	200	(Albert et al. 2006)
1ES 1218+304*	HBL	0.182	19.14	15	average	$3.08 \pm 0.34_{\rm stat} \pm 0.2_{\rm syst}$	7%	200	(Acciari et al. 2009c)
					VERITAS	$3.07 \pm 0.09_{\rm stat}$	6%	200	(Acciari et al. 2010b)
W Comae*	IBL	0.102	14.84	47	high	$3.81 \pm 0.35_{\rm stat} \pm 0.34_{\rm syst}$	9%	200	(Acciari et al. 2008)
PKS 1222+21 (4C +21.35)	FSRQ	0.432	13.27	101	MAGIC	$3.75 \pm 0.27_{\rm stat} \pm 0.2_{\rm syst}$	100%	100	(Aleksić et al. 2011b)
3C 279	FSRQ	0.536	12.67	898	high	$4.1 \pm 0.7_{\rm stat} \pm 0.2_{\rm syst}$	15%	200	(Albert et al. 2008)
PKS 1424+240	IBL	0.260[b]	15.7	26	VERITAS	$3.80 \pm 0.5_{\rm stat} \pm 0.3_{\rm syst}$	3%	140	(Acciari et al. 2010a)
H 1426+428	HBL	0.129	18.55	7	average	···	3%	1000	(Horns et al. 2004)
PG 1553+113	HBL	0.4[c]	16.49	44	high	$3.4 \pm 0.1_{\rm stat} \pm 0.2_{\rm syst}$	8%	200	(Aleksić et al. 2010)
Markarian 501*	HBL	0.034	16.84	46	low	$2.79 \pm 0.12_{\rm stat}$	20%	200	(Anderhub et al. 2009b)
1ES 1959+650*	HBL	0.048	18.03	16	low	$2.58 \pm 0.18_{\rm stat}$	10%	200	(Tagliaferri et al. 2008)
PKS 2005-489*	HBL	0.071	···	9	average	$3.20 \pm 0.16_{\rm stat} \pm 0.10_{\rm syst}$	3%	400	(Acero et al. 2010)
PKS 2155-304*	HBL	0.117	15.7	63	HESS	$3.34 \pm 0.05_{\rm stat} \pm 0.1_{\rm syst}$	14%	400	(Aharonian et al. 2009)
					low	$3.53 \pm 0.06_{\rm stat} \pm 0.10_{\rm syst}$	15%	200	(Abramowski et al. 2010b)
BL Lacertae	LBL	0.069	14.28	35	high	$3.64 \pm 0.54_{\rm stat} \pm 0.2_{\rm syst}$	3%	200	(Albert et al. 2007c)
1ES 2344+514*	HBL	0.044	16.4	10	average	$2.95 \pm 0.12_{\rm stat} \pm 0.2_{\rm syst}$	11%	200	(Albert et al. 2007a)
H 2356-309	HBL	0.165	17.24	8	average	$3.06 \pm 0.15_{\rm stat} \pm 0.10_{\rm syst}$	2%	240	(Abramowski et al. 2010a)

Notes. Columns (1), (2), and (3) show the spectral energy distribution (SED) type, redshift, and synchrotron peak frequency ($\nu_{\rm syn}$), respectively. *Fermi* variability indices (4) were taken from the 1FGL catalog (Abdo et al. 2010b). *Fermi* states (5) are identified in this work using 27-month *Fermi* light curves as described in Section 5. In cases where *Fermi* data are contemporaneous with TeV observations, the corresponding TeV instruments are listed in Column (5). TeV spectral indices (6) were taken from the references listed (9). TeV integral fluxes (7) are above the listed energy threshold (8) and in units of Crab Nebula flux. For the Crab Nebula unit conversions, spectral measurements above 350 GeV from Çelik (2008) are used.

[a] Miller et al. (1978); Lanzetta et al. (1993).

[b] Prandini et al. (2011).

[c] Mazin & Goebel (2007).

[*] Blazars that are reported as variable in the TeV band, according to TeVCat (http://tevcat.uchicago.edu/).

For VHE data that were taken during the *Fermi* era, time periods of a few months that cover the corresponding VHE observations were selected for the *Fermi* spectral analysis. For blazars that have VHE spectra measured before the *Fermi* era, the first 27 months of *Fermi* data were analyzed (from 2008 August 4 to 2010 November 4). In all the analysis steps, an energy selection from 300 MeV to 100 GeV was applied to the data.

The *Fermi* data were analyzed in the following way. First, a 27-month light curve analysis was performed for each source using an aperture photometry technique. *Diffuse class* events from a region of 1° radius from the target location were selected and counts were plotted as a function of time, each time bin containing 49 counts, corresponding to a signal to noise ratio of 7. For sources with high statistics, low- and high- flux states were identified and separated using the average count rate as a threshold. Figure 7 shows the resulting light curves for all sources, with fluxes normalized to arbitrary units. It should be noted that in this analysis, no background subtraction was performed and therefore the resulting light curves merely give an estimate of high- and low-state time slices.

Next, a spectral analysis was done for each data set. *Diffuse class* events from a region of interest of 8° radius were selected and analyzed with Fermi Science Tools v9r18p6,[7] using instrument response functions P3_V6_DIFFUSE. Sources from the first *Fermi*-LAT (1FGL) catalog (Abdo et al. 2010b), bright spots with test statistics >25 and standard galactic and isotropic

---

[7] http://fermi.gsfc.nasa.gov/ssc/data/analysis/scitools/overview.html

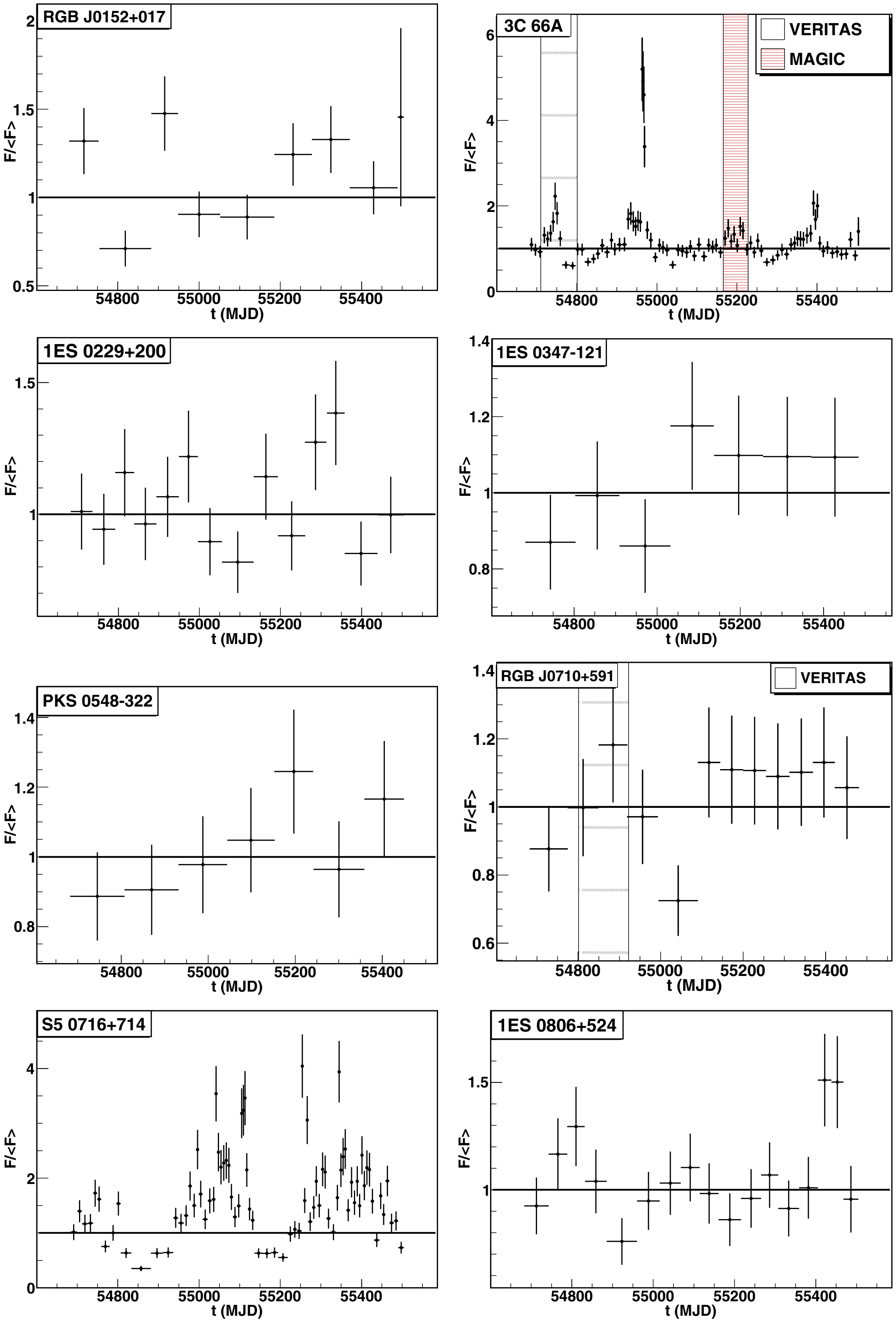

Figure 7. *Fermi*-LAT aperture photometry light curves with no background subtraction, normalized to arbitrary units. The solid lines, representing the average counts per area per time, separate "low" and "high" flux states, that are later on used to produce "low" and "high" state spectra. In the case of Markarian 421 and 3C 279 light curves, the dashed lines represent 1 σ deviation from the average, dividing the data set into three separate flux states ("low," "medium," and "high"). The shaded areas show the contemporaneous time windows with the corresponding TeV instruments.

(A color version of this figure is available in the online journal.)

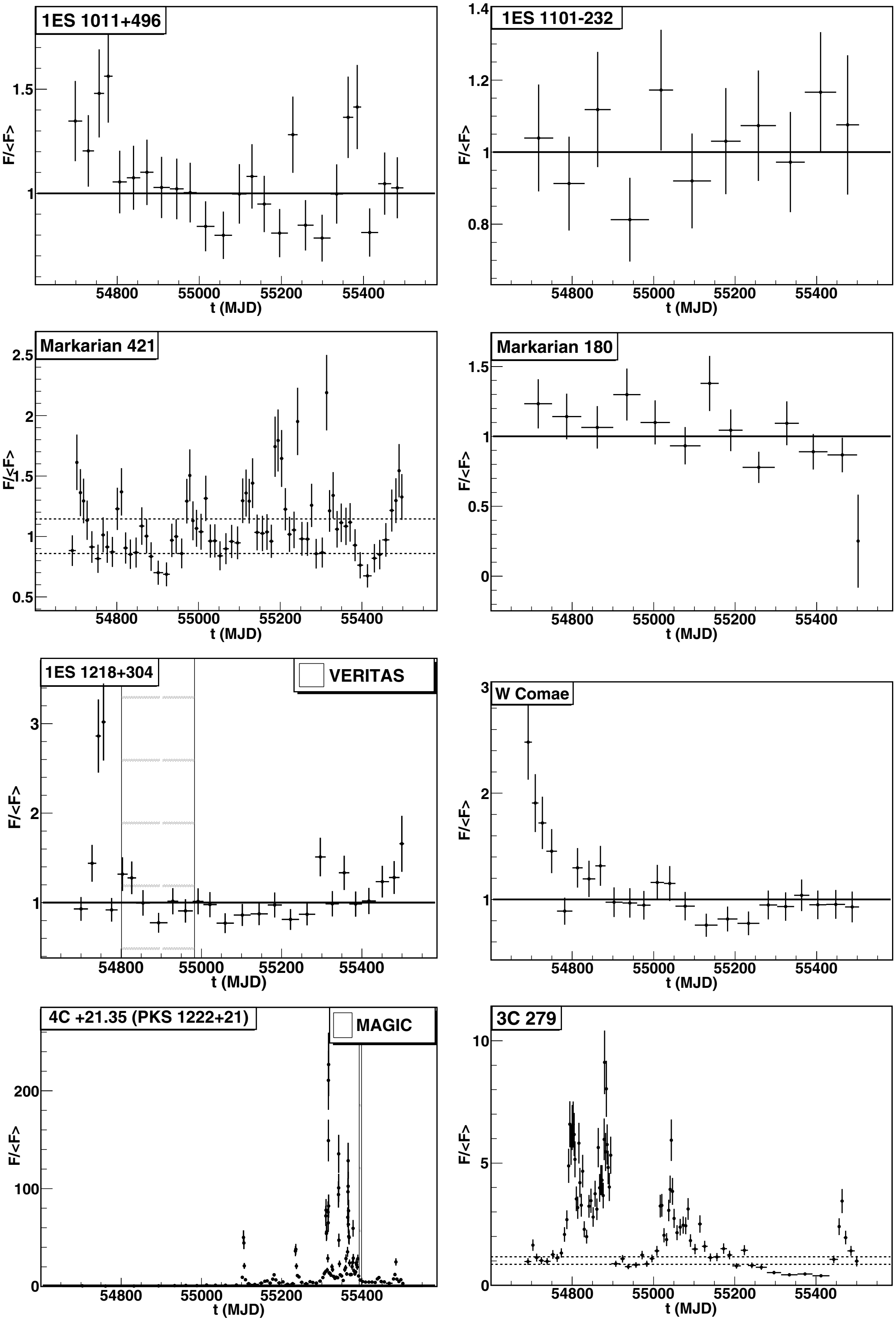

Figure 7. (Continued)

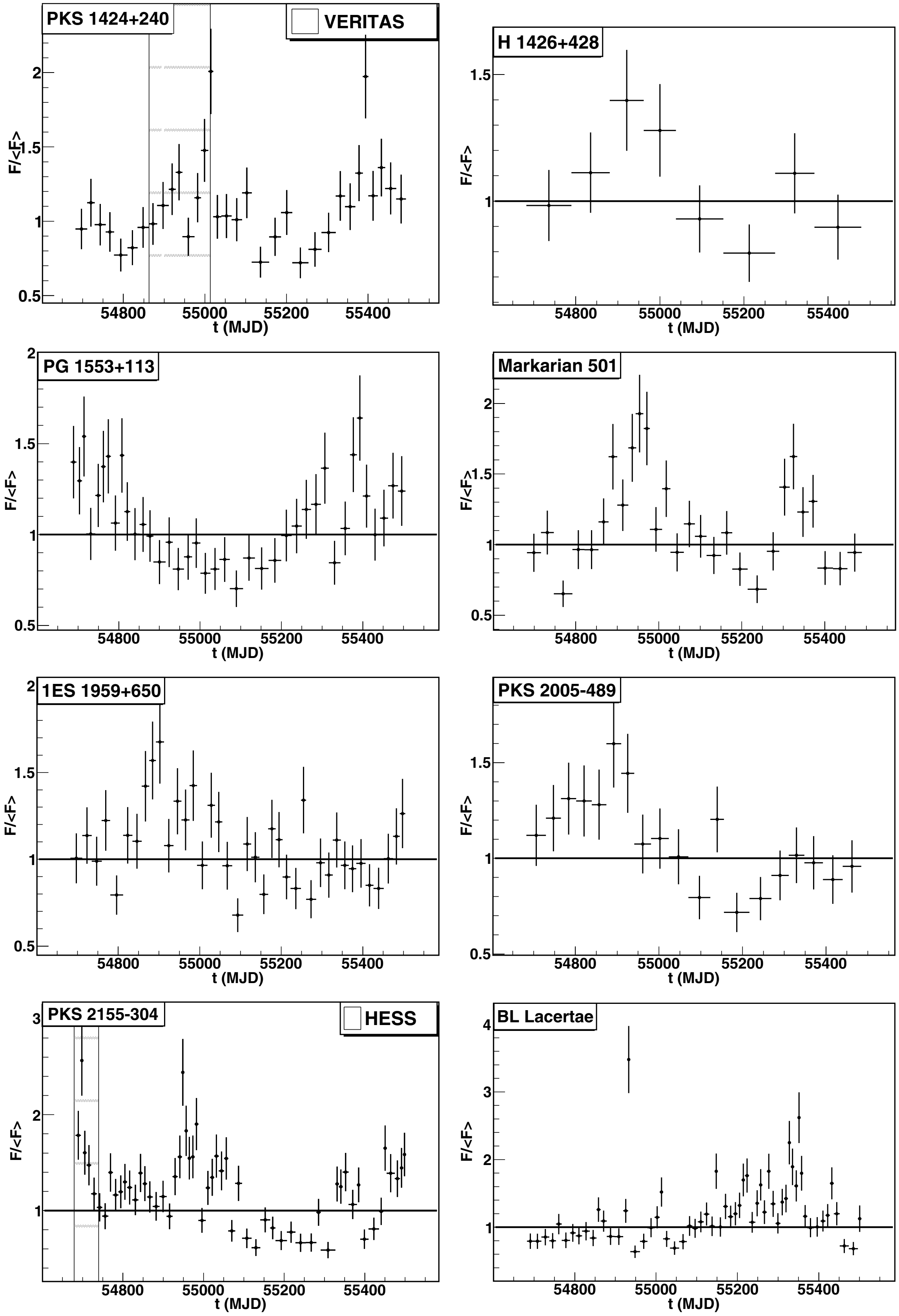

Figure 7. (Continued)

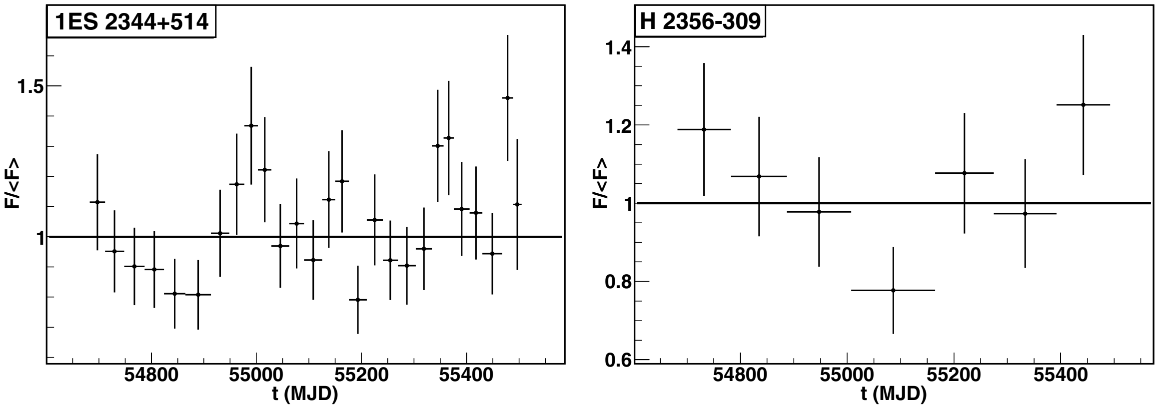

Figure 7. (Continued)

diffuse emission background components[8] within the region of interest were included in the source model files. Unbinned maximum-likelihood analysis as described in Cash (1979); Mattox et al. (1996) was applied to each data set, assuming a power-law (PL) spectrum as given in Equation (2).

$$dN/dE = N_0(E/E_0)^{-\Gamma}. \tag{2}$$

Additionally, to look for possible spectral features in the data, spectral points were calculated and fitted with different power-law functions, and the results were compared. See Section 6.4 for more details.

Finally, combined GeV–TeV SED data sets were constructed using archival TeV spectra and the corresponding flux state information from references shown in Table 1. With each TeV spectrum, the most suitable *Fermi* data subset (average, low- or high- state) was used for further study.

6. RESULTS AND DISCUSSION

Out of 26 blazars, 12 did not have enough statistics for a temporal separation of the *Fermi* data set into different flux states. Therefore for this subsample, an average spectrum was calculated using the entire data set. Data from another subsample with 12 blazars were split into high and low-flux states as described in Section 5. Data from the two brightest blazars (Markarian 421 and 3C 279) were split into three subsets, with low, medium, and high-flux states. See Table 2 for a summary of our *Fermi* data analysis results.

Our analysis results are consistent with the 2FGL catalog (Nolan et al. 2012). We used the combined GeV–TeV SEDs (see Figure 8) to estimate the IC peak frequency band of each blazar (see Section 6.1). Our sample contains a handful of candidate "TeV-peaked" blazars that we discuss in Section 6.2. In addition, considering the fact that *Fermi* spectral indices do not vary significantly between low- and high-states, we studied the change in spectral index from GeV to TeV as a function of the redshift, thus confirming the EBL effect on TeV spectra with a model-independent approach (see Section 6.3). On the other hand, interesting spectral features in the GeV band are observed. To probe these features, the data were fitted with three different functions and the corresponding fit improvements were calculated (see Section 6.4). Finally, in Section 6.5, we extended this study to contemporaneous combined SEDs.

6.1. IC Peak Frequency

The peak frequency of the IC component is a salient parameter for describing blazar non-thermal continua and studying population trends. Systematic studies for measuring the IC peak frequency mostly suffer from the lack of statistics and simultaneous data. A similar work was carried out in Zhang et al. (2012), where archival multiwavelength data were used to model TeV blazar SEDs and determine the IC peak frequency (ν_{IC}). A positive correlation between ν_{syn} and ν_{IC} was reported. In this work, we focus on finding the IC "peak frequency band" rather than the "peak frequency," using a model-independent approach. For each blazar SED shown in Figure 8, we identify the energy decade in which the largest amount of power is emitted. Note that the spectral points used in the VHE spectra are EBL-corrected. Figure 9 shows the distribution of the IC peak bands for different blazar types. We observe that the FSRQs, LBLs and IBLs have the maximum of their emission mostly below 1 GeV. On the other hand, HBLs tend to peak in the TeV range. This positive correlation between the synchrotron (ν_{syn}) and the IC peak frequencies (ν_{IC}) is in accordance with simple SSC models that predict a positive correlation between ν_{syn} and ν_{IC} (Abdo et al. 2010a). The dashed lines represent the same distributions with the bright AGN sample from the first three months of *Fermi* data (Abdo et al. 2010a). Our results tend to span the high frequency sides of all distributions and one clearly sees a shift to higher frequencies in the case of HBLs. This is expected since our sample consists of TeV-selected objects that mostly correspond to relatively weak sources in the GeV data and are therefore less likely to appear in a bright AGN sample. It should also be noted that we use a model independent method using only *Fermi* and VHE data, whereas (Abdo et al. 2010a) uses multiwavelength data and some modeling in cases where the soft X-ray band is dominated by the synchrotron component, a typical feature for our blazar sample.

6.2. Hard TeV BL Lac Objects

The combined GeV–TeV spectra of some blazars in our sample (1ES 0229+200, 1ES 0347-121, 1ES 1101-232, 1ES 1218+304, H 1426+428) suggest a ν_{IC} beyond ~1 TeV. These blazars are mostly weak or non-detected in the *Fermi* range, with a hard spectral index in both GeV and TeV bands. It follows that they may belong to the so-called ultra-high-frequency-peaked BL Lac subclass (UHBLs; see, e.g., Costamante 2011) that would constitute the extreme end of the population, and is expected to dominate the TeV luminosity of the universe. Several mechanisms have been set forth to explain the formation

---

[8] http://fermi.gsfc.nasa.gov/ssc/data/access/lat/BackgroundModels.html

Table 2
Fermi Analysis Results for the Sample

Name	SED Type (1)	z (2)	F_{var} (3)	*Fermi* State (4)	Γ_{GeV} (5)	$F_{1-100}(\mathrm{cm}^{-2}\,\mathrm{s}^{-1})$ (6)	TS (7)	Live Time (day) (8)
RGB J0152+017	HBL	0.080	0.19	average	2.09 ± 0.14	$(7.70 \pm 1.26) \times 10^{-10}$	106	822
3C 66A*	IBL	0.444[a]	0.59	MAGIC	2.09 ± 0.06	$(2.41 \pm 0.19) \times 10^{-8}$	953	62
				VERITAS	1.91 ± 0.05	$(2.50 \pm 0.16) \times 10^{-8}$	1485	91
1ES 0229+200	HBL	0.140	0.07	average	2.23 ± 0.34	$(2.96 \pm 1.07) \times 10^{-10}$	21	822
1ES 0347-121	HBL	0.188	<0.12	average	0.85 ± 0.54	$(5.33 \pm 3.90) \times 10^{-11}$	16	822
PKS 0548-322	HBL	0.069	<0.14	average	1.65 ± 0.25	$(2.93 \pm 1.00) \times 10^{-10}$	40	822
RGB J0710+591	HBL	0.125	<0.11	VERITAS	1.44 ± 0.33	$(9.94 \pm 4.09) \times 10^{-10}$	33	121
S5 0716+714	LBL	0.300	0.44	high	2.13 ± 0.04	$(2.01 \pm 0.09) \times 10^{-8}$	3644	342
1ES 0806+524	HBL	0.138	0.13	average	1.77 ± 0.07	$(1.45 \pm 0.14) \times 10^{-9}$	400	822
1ES 1011+496	HBL	0.212	0.15	high	1.97 ± 0.04	$(7.82 \pm 0.47) \times 10^{-9}$	1705	332
1ES 1101-232	HBL	0.186	<0.10	average	1.88 ± 0.26	$(4.59 \pm 1.27) \times 10^{-10}$	47	822
Markarian 421*	HBL	0.031	0.22	medium	1.78 ± 0.02	$(2.64 \pm 0.08) \times 10^{-8}$	7943	350
Markarian 180	HBL	0.046	0.22	average	1.87 ± 0.08	$1.22 \pm 0.12 \times 10^{-9}$	356	822
1ES 1218+304	HBL	0.182	0.44	average	1.69 ± 0.06	$(2.80 \pm 0.23) \times 10^{-9}$	708	822
				VERITAS	1.84 ± 0.11	$(3.30 \pm 0.49) \times 10^{-9}$	187	182
W Comae*	IBL	0.102	0.32	high	2.07 ± 0.06	$(8.34 \pm 0.59) \times 10^{-9}$	1101	222
PKS 1222+21	FSRQ	0.432	1.42	MAGIC	2.17 ± 0.04	$(7.24 \pm 0.47) \times 10^{-6}$	4267	6
3C 279	FSRQ	0.536	0.65	high	2.37 ± 0.02	$(5.25 \pm 0.15) \times 10^{-8}$	13558	218
PKS 1424+240	IBL	0.260[b]	0.22	VERITAS	1.85 ± 0.05	$(1.21 \pm 0.09) \times 10^{-8}$	1116	150
H 1426+428	HBL	0.129	0.07	average	1.12 ± 0.16	$(4.05 \pm 0.86) \times 10^{-10}$	197	822
PG 1553+113	HBL	0.4[c]	0.16	high	1.74 ± 0.03	$(1.66 \pm 0.07) \times 10^{-8}$	3339	344
Markarian 501*	HBL	0.034	0.25	low	1.84 ± 0.05	$(5.78 \pm 0.36) \times 10^{-9}$	1280	458
1ES 1959+650*	HBL	0.048	0.14	low	2.04 ± 0.06	$(4.45 \pm 0.30) \times 10^{-9}$	834	443
PKS 2005-489	HBL	0.071	0.15	average	1.82 ± 0.05	$(3.37 \pm 0.23) \times 10^{-9}$	834	822
PKS 2155-304*	HBL	0.117	0.29	HESS	1.89 ± 0.05	$(3.20 \pm 0.24) \times 10^{-8}$	1308	61
				low	1.95 ± 0.03	$(1.55 \pm 0.06) \times 10^{-8}$	4118	420
BL Lacertae	LBL	0.069	0.37	high	2.34 ± 0.04	$(1.52 \pm 0.07) \times 10^{-8}$	2517	283
1ES 2344+514*	HBL	0.044	0.09	average	1.97 ± 0.07	$(2.09 \pm 0.19) \times 10^{-9}$	407	822
H 2356-309	HBL	0.165	0.04	average	2.40 ± 0.18	$(5.63 \pm 0.81) \times 10^{-10}$	108	822

Notes. Columns (1) and (2) are the same as in Table 1. F_{var} (3) is the calculated flux variability amplitude (see Section 6.3) for the 27-month period. *Fermi* states (4) are as described in Section 5. In cases where *Fermi* data are contemporaneous with TeV observations, the corresponding TeV instruments are listed in Column (4). Γ_{GeV} (5) represents the photon index and F_{1-100} (6) the integral flux for 1–100 GeV. Test statistics (TS) and live time corresponding to the listed flux state are given in Columns (7) and (8), respectively.

[a] Miller et al. (1978); Lanzetta et al. (1993).

[b] Prandini et al. (2011).

[c] Mazin & Goebel (2007).

* Blazars that are reported as variable in the TeV band, according to TeVCat (http://tevcat.uchicago.edu/).

of these hard γ-ray spectra (Lefa et al. 2011). Extensive spectral analysis of these objects would be valuable for EBL and intergalactic magnetic field measurements. It should be noted that at energies of a few TeV and beyond, our spectra become EBL-model-dependent. For this reason, we have compared our adopted EBL model with two other models from recent studies (Finke et al. 2010; Franceschini et al. 2008). We have found that for the data samples mentioned above, if we used any of the other two EBL models, the dispersion in the highest energy flux points would be less than 20%, and consequently the observed spectral upturns would not be affected significantly.

With additional data, a deeper variability study carried on these blazars would relate to arguments that support the cosmic ray production as the origin of TeV blazar emission, since in that scenario no short timescale variability would be expected to be observed (Murase et al. 2012). Among the UHBL candidates, the ones that are present in the 1FGL catalog (1ES 1101-232, 1ES 1218+304, H 1426+428) have relatively small *Fermi* variability indices (see Table 1). In addition to that, our calculations of F_{var} for all five blazars using 27 months of *Fermi* data do not indicate a significant hint of variability either (see Table 2).

6.3. Spectral Variability

VHE emission from blazars is highly variable. This variability, manifested in irregular flares, is one of the most typical and promising blazar behaviors for studying the nature of underlying emission mechanisms. The observed flux change during a

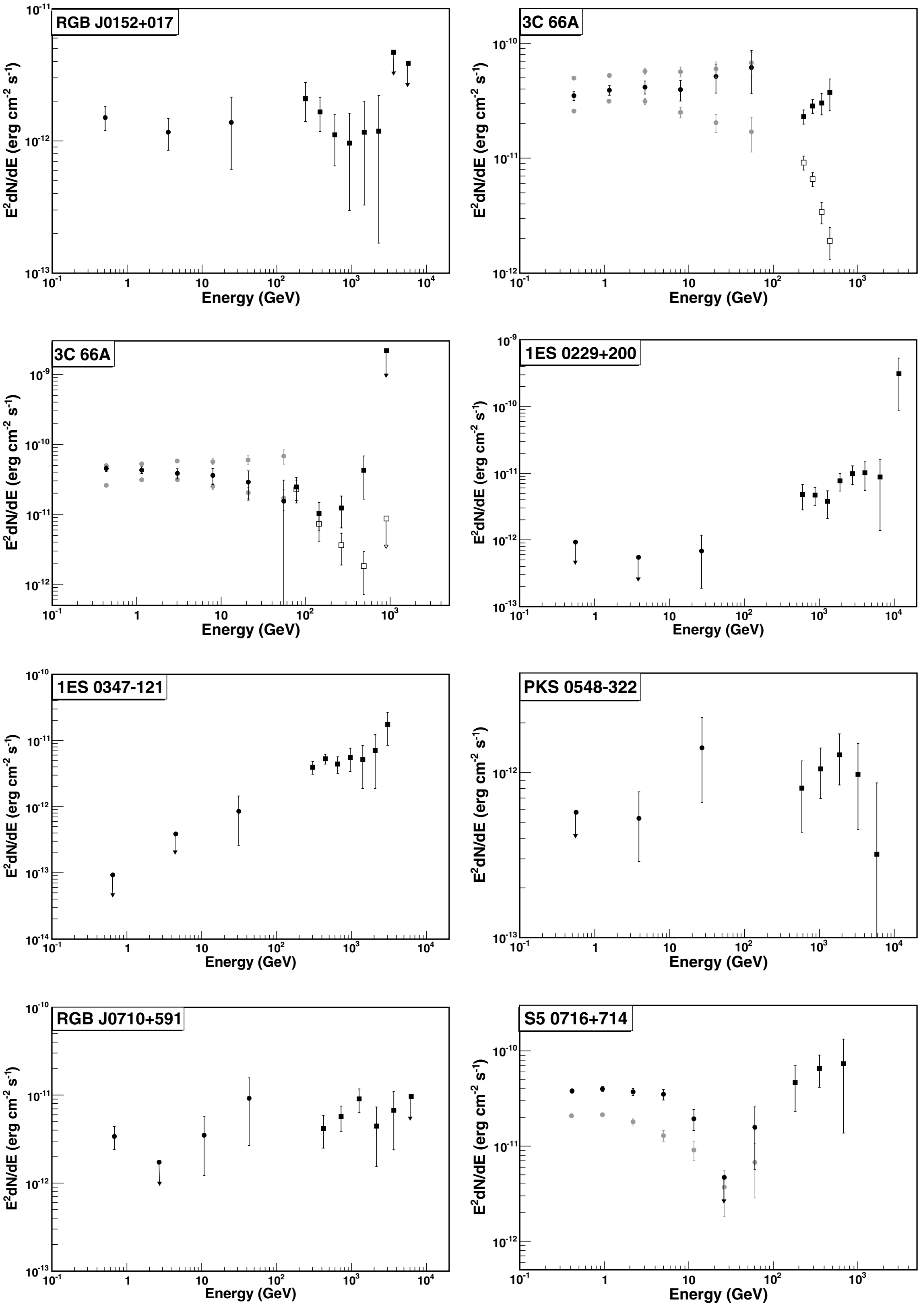

Figure 8. GeV–TeV spectra for the sample of blazars in this study. The filled circles represent the *Fermi* spectra and the filled squares the TeV spectra. Considering the TeV flux state information given in the TeV papers, the best matching GeV and TeV spectral points are used for the combined analysis (shown in black). When available, spectral points belonging to other flux states (in both bands) are plotted in gray. 3C66A (VERITAS and MAGIC, respectively), RGB J0710+591, 1ES 1218+304, 1222+21 (4C+21.35) (VERITAS), PKS 1424+240, PKS 2155-304 spectra are quasi-simultaneous.

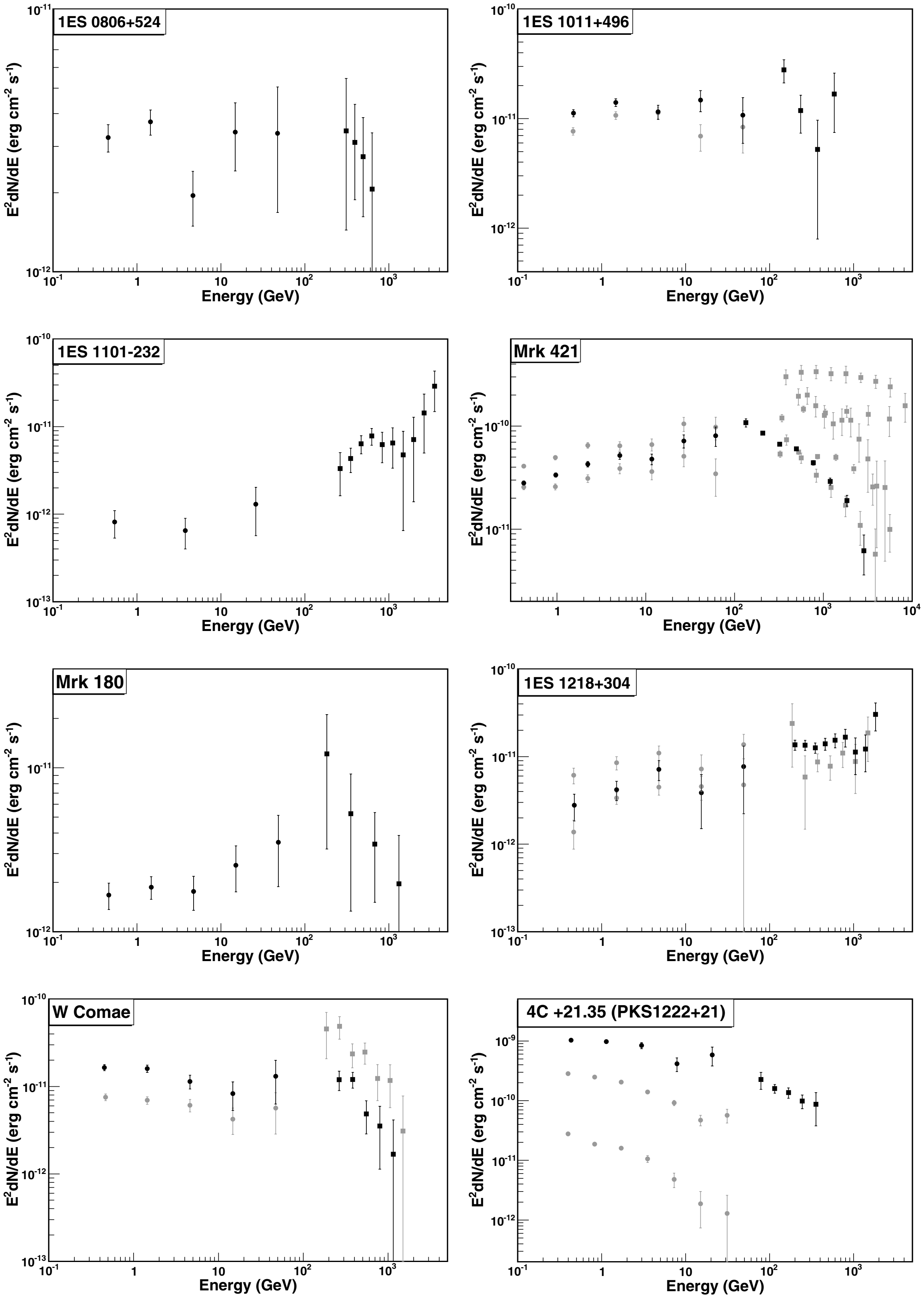

Figure 8. (Continued)

VHE flare can be as rapid as minute scales (Mkn 501: Albert et al. 2007e) and as large as 40 times the baseline emission (Arlen et al. 2013). Blazars that have been reported to have a variable flux are marked with an asterisk in Table 1. On the other hand, *Fermi* data do not exhibit flux variability as extreme as in the VHE band. In fact, having a smaller effective area than the ground-based VHE telescopes and operating mostly in survey mode rather than pointing, *Fermi*-LAT does not have the sensitivity to probe sub-hour timescale variability in blazars. Still, a possible correlation between GeV and TeV emission

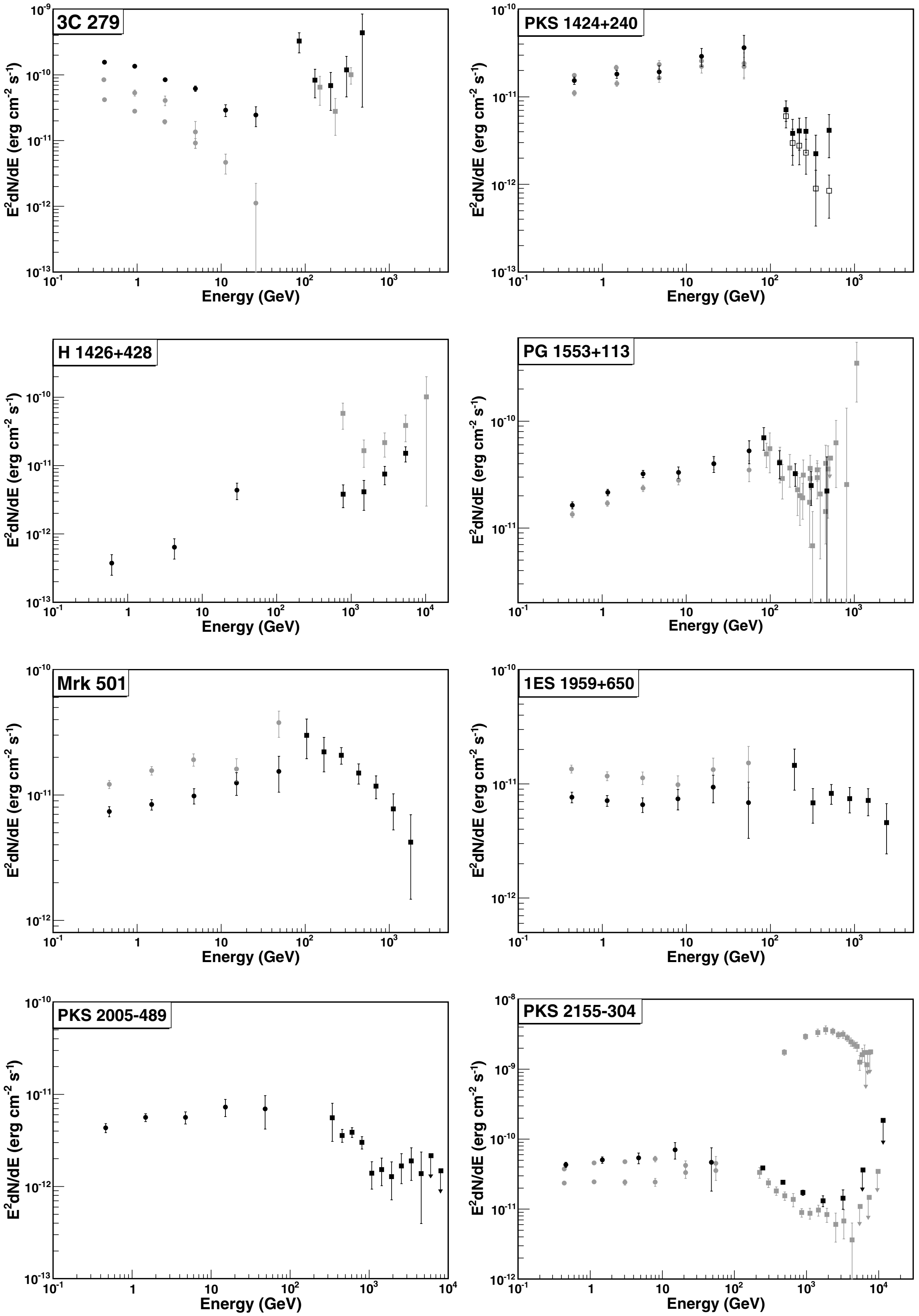

Figure 8. (Continued)

remains viable (Abdo et al. 2011; Aleksić et al. 2011b) and an enhanced activity in the high-energy tail of the *Fermi* band could therefore indicate a TeV flare. In this frame, monitoring GeV flares to trigger TeV observations is important (Errando et al. 2011a) and potentially could help in probing fast variability. To examine variability within the *Fermi* data, we compared high- and low-state *Fermi* spectra from 14 blazars (see Table 3). Half of these blazars have their integral flux in 1–100 GeV

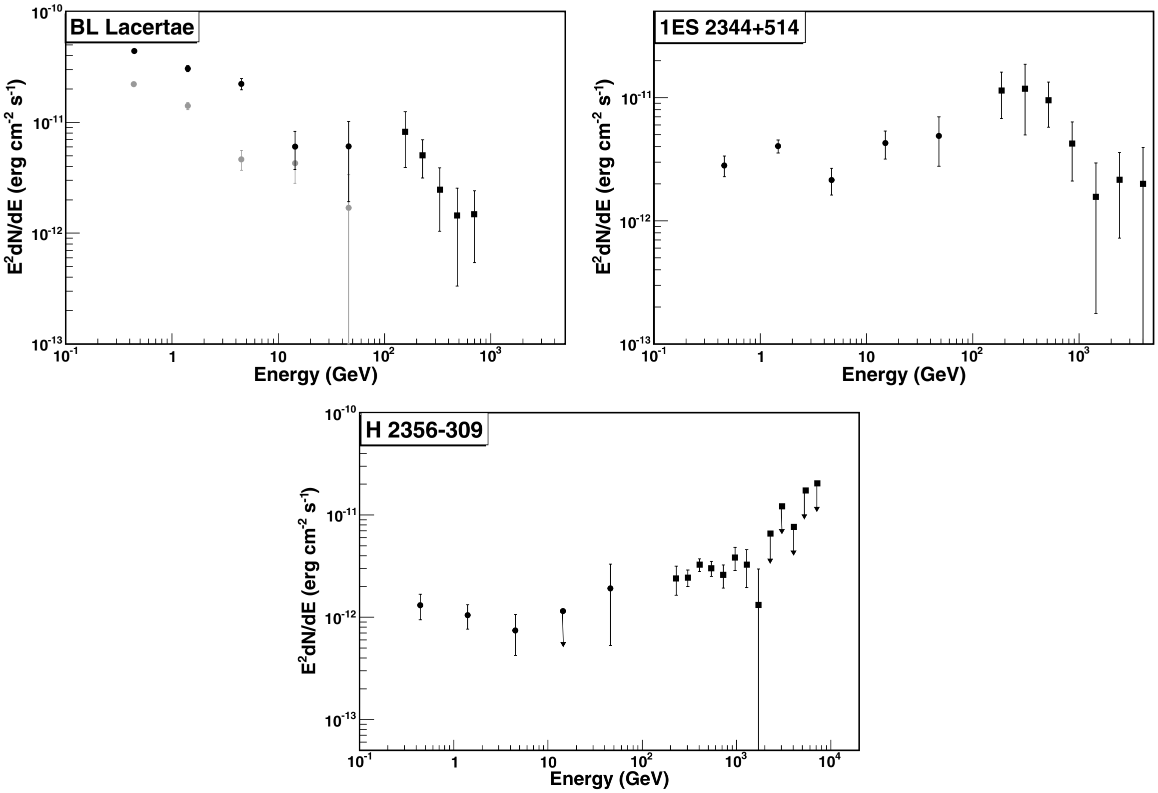

Figure 8. (Continued)

Table 3
Spectral Variations in the *Fermi* Data for Blazars for Which at Least Two Different *Fermi* Flux States are Available

Name	SED Type (1)	Increase in F_{1-100} (%) (2)	Γ_{low} (3)	Γ_{high} (4)
3C66A	IBL	95	2.00 ± 0.02	1.93 ± 0.02
S5 0716+714	LBL	100	2.20 ± 0.03	2.13 ± 0.04
1ES 1011+496	HBL	30	1.90 ± 0.04	1.97 ± 0.04
Mrk 421	HBL	90	1.86 ± 0.03	1.79 ± 0.02
1ES 1218+304	HBL	60	1.68 ± 0.08	1.73 ± 0.10
W Comae	IBL	110	2.10 ± 0.06	2.07 ± 0.06
PKS 1222+21	FSRQ	1290	2.50 ± 0.04	2.32 ± 0.02
3C 279	FSRQ	395	2.54 ± 0.03	2.37 ± 0.02
PKS 1424+240	IBL	45	1.82 ± 0.04	1.87 ± 0.03
PG 1553+113	HBL	30	1.70 ± 0.03	1.74 ± 0.03
Mrk 501	HBL	80	1.84 ± 0.05	1.83 ± 0.04
1ES 1959+650	HBL	60	2.04 ± 0.06	2.07 ± 0.05
PKS 2155-304	HBL	80	1.95 ± 0.03	1.92 ± 0.02
BL Lacertae	LBL	140	2.46 ± 0.05	2.34 ± 0.04

Notes. Column (1) shows the spectral energy distribution (SED) type. F_{1-100} is the integral flux for the 1–100 GeV band. Column (2) shows the percent increase in F_{1-100} from low to high *Fermi* state. FSRQs and LBLs seem to show the most significant flux variability in this energy range. Columns (3) and (4) list the GeV photon indices in low and high *Fermi* states, respectively. No significant changes in photon index are seen, except for the two FSRQs for which the index shows a slight hardening from low to high flux states.

(F_{1-100}) increased by at least 90% in the high state. The largest flux increase is seen in the case of the two FSRQs 3C 279 and PKS 1222+21. As depicted by their respective light curves in Figure 7, these two objects have undergone dramatic GeV flares. Such a large-scale flux increase does not hold for the remainder of the blazars. However, one should keep in mind that for most of the TeV blazars, the *Fermi* band is a relatively stable region of the SED, since it samples the low energy part of the parent electrons, that have a longer cooling time. Table 3 gives a summary of the results of the spectral variations seen in the *Fermi* data. We also calculated the variability amplitude (F_{var}) within 27 months of *Fermi* data for each blazar, using the method described in Vaughan et al. (2003). F_{var} is a measure of the intrinsic source variance, calculated based on excess variance. For blazars with negative excess variance, 95% confidence level upper limits are given. The blazars 3C 66A, PKS 1222+21 and 3C 279 are the most variable ones according to this calculation ($F_{\mathrm{var}} > 0.5$). Our results are in agreement with the 1FGL catalog (see Table 1). Comparing these results with the TeV variability flags, we do not find any obvious relation between GeV and TeV variabilities (see Table 2).

Within the *Fermi* energy range, blazars in our sample do not exhibit dramatic changes in their spectral index between different flux states (see Table 3). Consequently, this makes the photon index a reasonable parameter to use for studying the non-contemporaneous combined SEDs. Figure 10 shows a scatter plot of observed Γ_{TeV}–Γ_{GeV} versus redshift. A constant function does not provide a good description for the data, with $\chi^2/\mathrm{dof} = 204/27$, which could be interpreted as a model-independent indication for the EBL absorption. The difference between TeV and GeV photon indices increases with redshift. This is expected since the VHE γ-ray photons pair produce

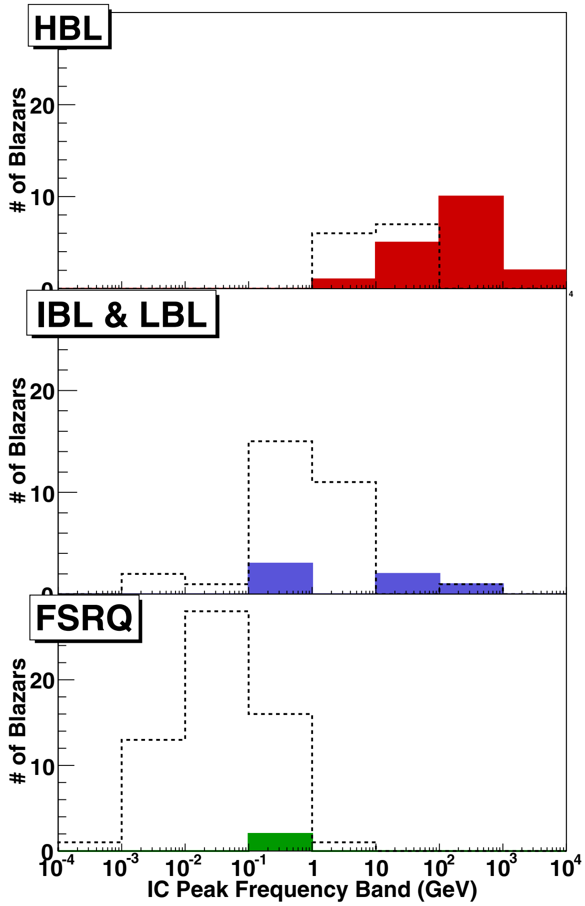

Figure 9. Distribution of the IC peak bands, defined as the energy decade in which the largest amount of power is emitted, in combined GeV–TeV spectra. Top, middle, and bottom panels show HBLs, IBLs+LBLs, and FSRQs, respectively. HBLs tend to peak at higher frequencies, in accordance with their respective synchrotron peak frequencies ν_{syn} (see Table 1), and a decreasing trend in IC peak bands from top to bottom panel is seen. The dashed lines represent the same distribution for the blazar sample from Abdo et al. (2010a).

(A color version of this figure is available in the online journal.)

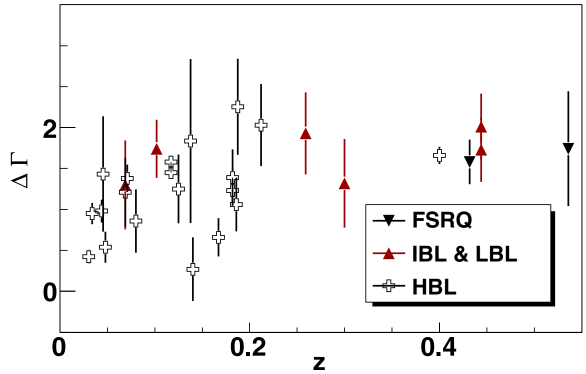

Figure 10. $\Delta\Gamma$ (Γ_{TeV}–Γ_{GeV}) vs. redshift. Empty crosses, triangles, and inverse triangles represent HBLs, IBLs+LBLs, and FSRQs, respectively. The fact that a constant function does not provide a good description for the data could be interpreted as a model independent indication for the EBL absorption.

(A color version of this figure is available in the online journal.)

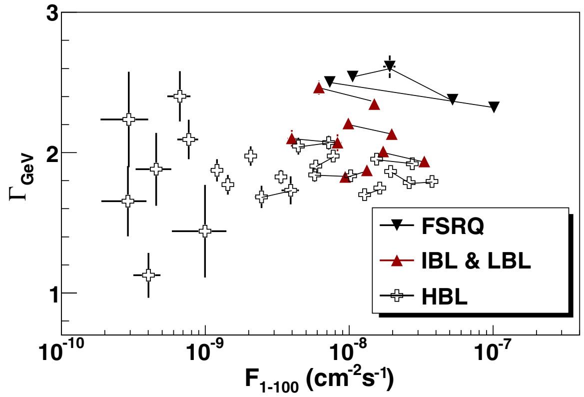

Figure 11. Γ_{GeV} vs. flux in the energy band 1–100 GeV from the analysis of 27 month *Fermi* data with a power-law fit (see Table 2). Empty crosses, triangles, and inverse triangles represent HBLs, IBLs+LBLs, and FSRQs, respectively. The solid lines connect different states of the same blazar.

(A color version of this figure is available in the online journal.)

with the EBL photons (Franceschini et al. 2008) and this effect becomes more enhanced at larger redshifts, making the universe opaque to TeV γ rays at distances larger than $z \sim 0.5$. HE spectra are not affected by the EBL, whereas VHE spectra become softer with increasing redshift. A similar observation was reported by Abdo et al. (2009), in a study carried out on a sample of TeV-selected AGNs detected with *Fermi*.

Figure 11 shows the relation between the spectral index Γ_{GeV} and the flux normalization F_{1-100} obtained from power-law fits. FSRQs and two subgroups of BL Lacs are clearly separated in the parameter space. This is in accordance with the aforementioned positive correlation trend between ν_{syn} and ν_{IC}, since 1 GeV typically corresponds to the rising edge of the IC component in an HBL SED, sampling a relatively low flux with hard spectral index. On the other hand for an FSRQ, 1 GeV will correspond to the peak or the falling edge of the IC component. The fact that FSRQs have relatively more luminous IC emission explains the softening trend with a larger normalization factor. However, the pattern that we observe between different flux states of a given blazar is the opposite. In most cases, a slight spectral hardening accompanies high flux states, indicating a change in the spectral shape and enhanced flux increase at high-energy tail of the spectrum.

6.4. Spectral Features

In most of the blazars in our sample, we observe interesting spectral features in the *Fermi* band, that appear as dips in the 1–100 GeV energy range. In an attempt to find a quantitative description for these features, we fit the *Fermi* spectral points with a simple power law (PL; Equation (2)) and a broken power law (BPL; Equation (3)), and then compare the results:

$$dN/dE = N_0 \times \begin{cases} (E/E_b)^{-\Gamma_1}, & E < E_b \\ (E/E_b)^{-\Gamma_2}, & \text{otherwise.} \end{cases} \qquad (3)$$

In the PL fit, the normalization N_0 and the spectral index Γ are free parameters, and the energy E_0 is fixed at 1 GeV. In the BPL fit, the break energy E_{b} and the indices Γ_1 and Γ_2, along with the normalization N_0 are free. In Table 4, we list the best-fit parameters from both functions and the likelihood ratio test results of BPL over PL. In 9 out of 33 cases, BPL yields a better fit over PL with more than 2σ significance.

There are several possible mechanisms that may cause the observed features in the SEDs. One possibility is a break in the electron spectrum caused by the synchrotron cooling effects, generally yielding a change in spectral index by 0.5 (Böttcher & Chiang 2002), which is in agreement with our results (see Table 4). Another mechanism that could explain the observed

Table 4
Fit Results for Power Law (PL) and Broken Power Law (BPL), Where BPL Yields a Better Fit Over PL with More Than 2σ Significance (9 Out of 33 Cases)

Name	Power Law		Broken Power Law				
	$N(\times 10^{-11})$ (1)	Γ (2)	$F_{1\mathrm{GeV}}(\times 10^{-12})$ (3)	Γ_1 (4)	Γ_2 (5)	E_{break} (GeV) (6)	σ_{BPL} (7)
3C66A (low)	2.78 ± 0.07	2.01 ± 0.02	9.30 ± 4.94	1.81 ± 0.06	2.22 ± 0.07	1.92 ± 0.51	4.12
S5 0716+714 (low)	1.85 ± 0.06	2.23 ± 0.03	5.18 ± 2.07	2.14 ± 0.04	2.74 ± 0.23	5.43 ± 1.01	3.07
S5 0716+714 (high)	3.68 ± 0.13	2.10 ± 0.03	2.29 ± 1.78	2.00 ± 0.06	2.57 ± 0.30	4.10 ± 1.47	2.29
1ES 1011+496 (low)	0.88 ± 0.04	1.94 ± 0.04	1.70 ± 1.34	1.70 ± 0.10	2.28 ± 0.20	2.76 ± 1.15	2.76
PKS 1222+21 (low)	1.72 ± 0.06	2.53 ± 0.04	0.99 ± 0.70	2.41 ± 0.06	3.11 ± 0.28	3.36 ± 0.87	2.84
3C 279 (low)	2.55 ± 0.08	2.59 ± 0.03	0.15 ± 0.28	2.53 ± 0.04	3.72 ± 1.54	7.70 ± 5.57	2.51
3C 279 (high)	1.16 ± 0.02	2.39 ± 0.02	8.14 ± 10.72	2.31 ± 0.03	2.74 ± 0.26	3.21 ± 1.79	3.11
PKS 2155-304 (low)	4.19 ± 0.10	1.92 ± 0.02	1.75 ± 1.98	1.86 ± 0.03	2.13 ± 0.14	5.54 ± 3.23	2.08
BL Lacertae (high)	3.26 ± 0.11	2.39 ± 0.04	1.08 ± 0.09	2.30 ± 0.04	3.00 ± 0.30	4.49 ± 0.03	2.50

Notes. Columns (1) and (2) show the PL parameters, flux normalization at 1 GeV and the photon index respectively. $F_{1\mathrm{GeV}}$ (3) is the flux normalization at 1 GeV for BPL. N and $F_{1\mathrm{GeV}}$ are in erg cm^{-2} s^{-1}. Columns (4) and (5) show the photon indices for BPL, as given in Equation (3). The break energy for BPL is listed in Column (6). σ_{BPL} (7) is the likelihood ratio test results of BPL over PL. For these 9 cases, the break energy E_{break} ranges from ~2 GeV to ~8 GeV. In addition, 7 of these data sets belong to non-HBL blazars.

breaks is the absorption by an external photon field (Poutanen & Stern 2010). For those nine data sets where the BPL gives a better fit than the PL, the break energy ranges from ~2 GeV to ~8 GeV. In addition, seven of these data sets belong to non-HBL blazars, that are usually characterized by broad emission lines, thought to be originating from a region of molecular gas (broad line region, BLR) that is highly ionized by the optically thin accretion disk. This seems in accordance with the idea of relating the *Fermi* spectral features to absorption of GeV photons on radiation from H I (13.6 eV) and He II (54.4 eV) recombination continua in the BLR, that are expected to cause jumps in γ-ray opacity around ~19.2 and ~4.8 GeV, respectively (Poutanen & Stern 2010). We tested a general absorbed power-law (APL) function of the following form on the *Fermi* data:

$$dN/dE = N_0(E/E_0)^{-\Gamma} e^{-\tau_{\gamma\gamma}(E, z, E_{\mathrm{abs}})}, \qquad (4)$$

where the free parameters are the normalization N_0 at $E_0 = 1$ GeV, photon index Γ, and absorption line energy E_{abs}. $\tau_{\gamma\gamma}$ is the optical depth for the γ–γ pair annihilation of photons with energies E and E_{abs} at a redshift of z. Within the *Fermi* energy band, BPL and APL functions fit the data equally well. Upturns at high-energy tails of *Fermi* spectra are observed (see, e.g., W Comae in Figure 8), but they are not statistically significant enough to favor an absorption scenario over a BPL fit. Therefore, it appears that one cannot statistically distinguish between the BPL and APL fits, but possible absorption scenarios are worth investigating further. To address this issue, we make use of contemporaneous GeV–TeV spectra to test and compare BPL and four different APL scenarios (see Section 6.5). This permits us to test the APL over a larger energy range and investigate the apparent *Fermi* spectral absorption-like features with higher statistics.

Another caveat related to these spectral features is that the upturn seen at the highest *Fermi* energy bin might be coming from a group of photons clustered in time. In that case the dip would be an artifact of a flaring event, thus not representative of the time-averaged spectrum. To make sure this is not the case, we checked the arrival times of the highest-energy photons and did not find any obvious clustering (see Figure 12). Note that the arrival time distributions should be considered within a given flux state. For instance, in the left panel of the figure, the red triangles represent the high energy photons from the high flux state and are evenly distributed in a time window that belongs to the high state. Therefore, one concludes that no clustering is found.

6.5. *Quasi-simultaneous GeV–TeV Spectra*

Seven of the TeV spectra in our sample are contemporaneous with *Fermi* observations and therefore merit a deeper analysis. We extended the work described in Section 6.4 to this subsample. This time, in addition to PL and BPL fits, we tested four different scenarios of absorption due to photons emitted from the BLR: H I line (13.6 eV), He II line (54.4 eV), H I and He II combined, and full BLR spectrum taken from Poutanen & Stern (2010).

For single- and double-line absorption scenarios, H I and He II recombination continua are the most plausible cases given that they are the most dominant ones in the BLR spectrum, and that the breaks we see in the *Fermi* spectra are located around a few GeV. As for the full BLR spectrum, taken from Poutanen & Stern (2010), it was modeled assuming a photoionized gas with the ionization parameter and the cloud density changing with the distance to the central ionizing source. See Poutanen & Stern (2010) for a detailed discussion on the γ-ray absorption within the BLR in the *Fermi* spectra. No general trend can be seen in the contemporaneous data sample. BPL and full BLR absorption scenarios seem to fit well the combined spectra of the blazars PKS 1424+240 and PKS 2155-304. A BPL (full BLR absorption) function is preferred over the PL for the blazars PKS 1424+240 and PKS 2155-304 with a significance of ~5σ (~4.8σ) and ~12σ (~8.5σ), respectively (see Figure 13). The χ^2/dof values of PL, BPL, and APL fits are 32/9, 3.5/7, and 5.3/7 for PKS 1424+240 and 148/8, 5.8/6, and 71/6 for PKS 2155-304, respectively. BPL fits yield $\Delta\Gamma = 1.4$ (PKS 1424+240) and $\Delta\Gamma = 0.7$ (PKS 2155-304), both larger than what electron cooling would predict, which might indicate that an additional mechanism is at work. Both BPL and full BLR absorption scenarios provide a slight improvement in the MAGIC and VERITAS spectra of 3C 66A, albeit not significant. Similarly, for PKS 1222+21, BPL, H I single line and H I + He II double line absorptions slightly improve the fit over PL. In the case of RGB J0710+091 and 1ES 1218+304, we don't observe any preference over the power-law fit. In case a γ–γ absorption from BLR is at work, the cascades initiated in this process might produce observable GeV γ-ray emission (Roustazadeh & Böttcher 2011), and their synchrotron emission could contribute

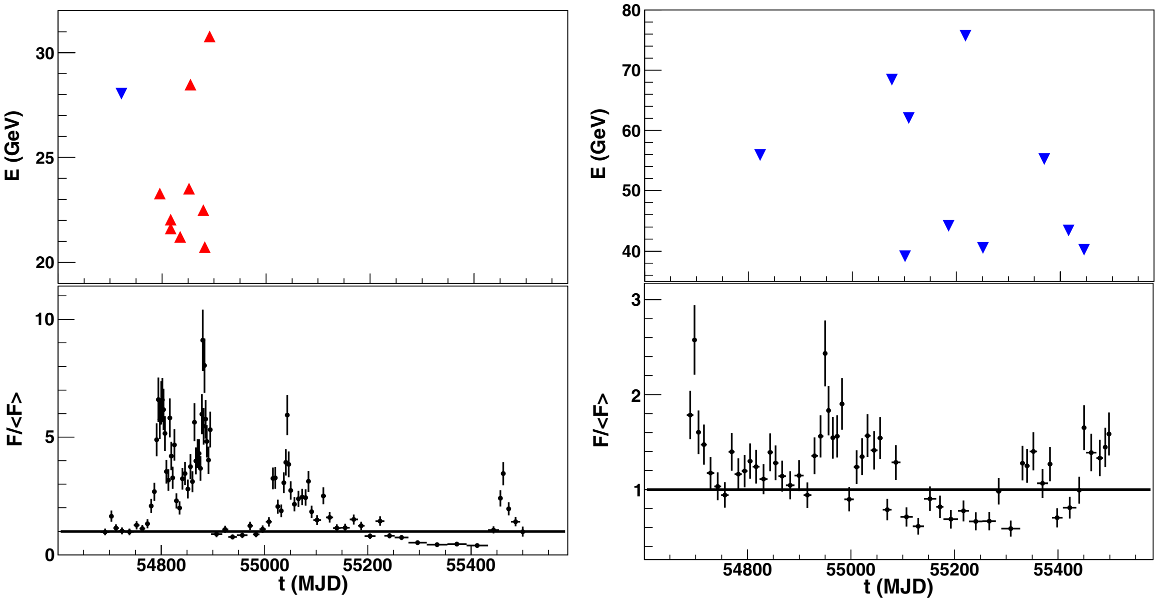

Figure 12. Arrival times of the photons in the highest energy bin (top panels) and aperture light curves with arbitrary flux units (bottom panels) for the blazars 3C 279 (left) and PKS 2155-304 (right). The blue upside-down triangles represent the low-state photons and red triangles the high-state ones. In both cases, the highest energy photons do not show any obvious clustering within their respective data sets. As described in Section 5, low- and high-states are distinguished based on the flux averages (solid lines) in light curves.

(A color version of this figure is available in the online journal.)

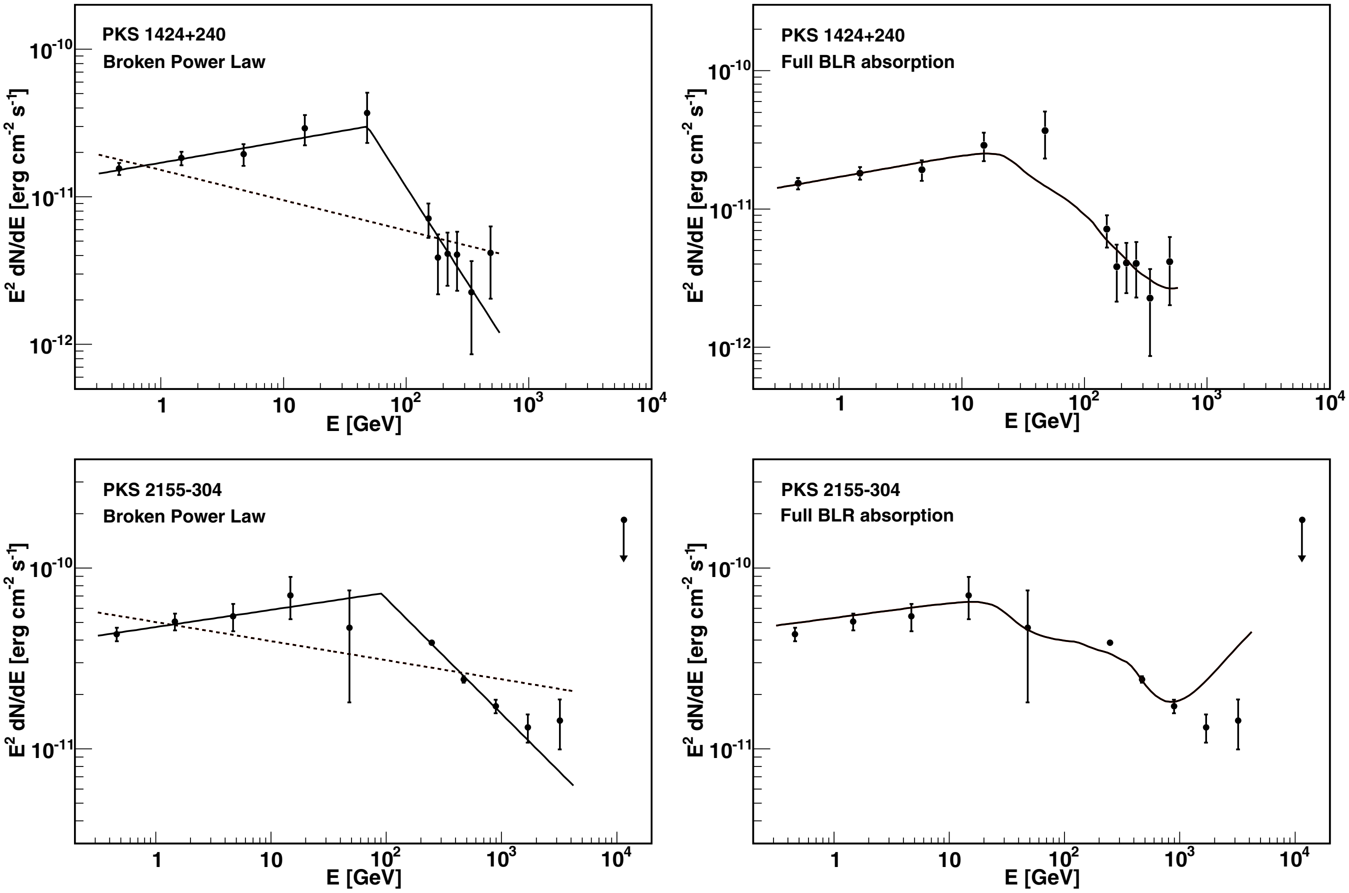

Figure 13. Contemporaneous GeV–TeV spectra with power-law (dashed lines), broken power-law (solid lines), and power-law with full-BLR-absorption fits. BPL and full BLR absorption scenarios seem to fit well the combined spectra of the blazars PKS 1424+240 and PKS 2155-304. A BPL (full BLR absorption) function is preferred over the PL for the blazars PKS 1424+240 and PKS 2155-304 with a significance of $\sim 5\sigma$ ($\sim 4.8\sigma$) and $\sim 12\sigma$ ($\sim 8.5\sigma$), respectively.

(A color version of this figure is available in the online journal.)

to the big blue bump seen in several blazars (Roustazadeh & Böttcher 2012).

7. SUMMARY

We study blazar spectral properties with a focus on the GeV–TeV energy range for a sample of VHE blazars. In order to obtain a set of joint GeV–TeV blazar spectra, we analyze the first 27-month *Fermi* data for VHE blazars and combine our results with archival VHE data. In cases where the *Fermi* data set does not overlap with the TeV observations but has enough statistics, we split the data into high and low flux states and join the best-matching subset with the corresponding TeV spectrum. The peak frequency band of the inverse Compton component increases following the order FSRQ -> LBL&IBL -> HBL. Thus, our results confirm the positive correlation between ν_{syn} and ν_{IC}. We note that *Fermi* spectra from different flux states for a given TeV blazar do not undergo a significant change in photon index. The variability amplitudes within our *Fermi* data set do not show an immediate correlation with the reported TeV variabilities for individual blazars. We find that in many cases a power law is insufficient to describe the GeV–TeV spectra and a broken power law improves the fits, especially for non-HBL blazars, where the BLR emission may have an effect on the observed spectral shape. In some blazars we observe absorption-like spectral features. We present seven quasi-simultaneous joint spectra, on which we test possible absorption scenarios from the BLR. Even though the absorption seems to describe well some of the observed spectra, no general pattern can be identified.

This work was supported in part by the NSF grant Phy-0855627 and NASA grant NNX09AU14G. We acknowledge Paolo Coppi for helpful discussions and Juri Poutanen for providing the BLR emission templates.

REFERENCES

Abdo, A. A., Ackermann, M., Agudo, I., et al. 2010a, ApJ, 716, 30
Abdo, A. A., Ackermann, M., Ajello, M., et al. 2009, ApJ, 707, 1310
Abdo, A. A., Ackermann, M., Ajello, M., et al. 2010b, ApJ, 715, 429
Abdo, A. A., Ackermann, M., Ajello, M., et al. 2011, ApJ, 726, 43
Abramowski, A., Acero, F., Aharonian, F., et al. 2010a, A&A, 516, 56
Abramowski, A., Acero, F., Aharonian, F., et al. 2010b, A&A, 520, 83
Acciari, V. A., Aliu, E., Arlen, T., et al. 2009a, ApJL, 690, L126
Acciari, V. A., Aliu, E., Arlen, T., et al. 2009b, ApJL, 693, L104
Acciari, V. A., Aliu, E., Arlen, T., et al. 2009c, ApJ, 695, 1370
Acciari, V. A., Aliu, E., Arlen, T., et al. 2010a, ApJ, 708, 100
Acciari, V. A., Aliu, E., Arlen, T., et al. 2010b, ApJ, 709, 163
Acciari, V. A., Aliu, E., Arlen, T., et al. 2010c, ApJL, 715, L49
Acciari, V. A., Aliu, E., Aune, T., et al. 2009d, ApJ, 707, 612
Acciari, V. A., Aliu, E., Beilicke, M., et al. 2008, ApJL, 684, L73
Acero, F., Aharonian, F., Akhperjanian, A. G., et al. 2010, A&A, 511, 52H
Aharonian, F., Akhperjanian, A. G., Anton, G., et al. 2009, ApJL, 696, L150
Aharonian, F., Akhperjanian, A. G., Anton, G., et al. 2010, A&A, 521, A69
Aharonian, F., Akhperjanian, A. G., Barres de Almeida, U., et al. 2007a, A&A, 473, L25
Aharonian, F., Akhperjanian, A. G., Barres de Almeida, U., et al. 2007b, A&A, 475, L9
Aharonian, F., Akhperjanian, A. G., Barres de Almeida, U., et al. 2008, A&A, 481, L103
Aharonian, F., Akhperjanian, A. G., Bazer-Bachi, A. R., et al. 2007c, A&A, 470, 475
Aharonian, F., Akhperjanian, A. G., Bazer-Bachi, A. R., et al. 2007d, ApJL, 664, L71
Aiso, S., Chikawa, M., Hayashi, Y., et al. 1997, in Proc. 25th International Cosmic Ray Conf., Vol. 5, ed. M. S. Potgieter, C. Raubenheimer, & D. J. van der Walt (Transvaal, South Africa: Potchefstroom Univ.), 373
Albert, J., Aliu, E., Anderhub, H., et al. 2006, ApJL, 648, L105
Albert, J., Aliu, E., Anderhub, H., et al. 2007a, ApJ, 662, 892
Albert, J., Aliu, E., Anderhub, H., et al. 2007b, ApJ, 663, 125
Albert, J., Aliu, E., Anderhub, H., et al. 2007c, ApJL, 666, L17
Albert, J., Aliu, E., Anderhub, H., et al. 2007d, ApJL, 667, L21
Albert, J., Aliu, E., Anderhub, H., et al. 2007e, ApJ, 669, 862
Albert, J., Aliu, E., Anderhub, H., et al. 2008, Sci, 320, 1752
Aleksić, J., Alvarez, E. A., Antonelli, L. A., et al. 2012, APh, 35, 435
Aleksić, J., Anderhub, H., Antonelli, L. A., et al. 2010, A&A, 515, A76
Aleksić, J., Antonelli, L. A., Antoranz, P., et al. 2011a, ApJ, 726, 58
Aleksić, J., Antonelli, L. A., Antoranz, P., et al. 2011b, ApJL, 730, L8
Anderhub, H., Antonelli, L. A., Antoranz, P., et al. 2009a, ApJL, 704, L129
Anderhub, H., Antonelli, L. A., Antoranz, P., et al. 2009b, ApJ, 705, 1624
Arlen, T., Anne, T., Beilicke, M., et al. 2013, ApJ, 762, 92
Armstrong, P., Chadwick, P. M., Cottle, P. J., et al. 1999, ExA, 9, 51A
Behera, B., & Wagner, S. J. 2009, arXiv:0908.4574B
Bernlöhr, K., Carrol, O., Cornils, R., et al. 2003, APh, 20, 111
Böttcher, M. 2010, in Fermi Meets Jansky, AGN at Radio and Gamma Rays, ed. T. Savolainen, E. Ros, R. W. Porcas, & J. A. Zensus (Bonn, Germany: Max-Planck Institut fur Radioastronomie), 41
Böttcher, M., & Chiang, J. 2002, ApJ, 564, 92
Cash, W. 1979, ApJ, 228, 939
Çelik, Ö. 2008, PhD dissertation, Univ. California, Los Angeles
Costamante, L., & Ghisellini, G. 2002, A&A, 384, 56
Costamante, L. 2011, Proc. 3rd Fermi Symp., Rome, Italy, eConf C110509
de la Calle Pérez, I., Bond, I. H., Boyle, P. J., et al. 2003, ApJ, 599, 909
Domìnguez, A., Primack, J. R., Rosario, D. J., et al. 2011, MNRAS, 410, 2556
Errando, M., Orr, M., & Kara, E. 2011a, Proc. 32nd ICRC, Beijing, China (arXiv:1110.1036)
Errando, M., for the VERITAS Collaboration 2011, Proc. 3rd Fermi Symp., Rome, Italy, eConf C110509
Finke, J. D., Razzaque, S., & Dermer, C. D. 2010, ApJ, 712, 238
Franceschini, A., Rodighiero, G., & Vaccari, M. 2008, A&A, 487, 837
Horns, D., Aharonian, F. A., & Costamante, L. 2004, NewA, 48, 387
Kadler, M., Eisenacher, D., Ros, E., et al. 2012, A&A, 538L, 1K
Kembhavi, A. K., & Narlikar, J. V. 1999, Quasars and Active Galactic Nuclei: An Introduction (Cambridge: Cambridge Univ. Press)
Kildea, J., Atkins, R. W., Badran, H. M., et al. 2007, APh, 28, 182
Lanzetta, K. M., Turnshek, D. A., & Sandoval, J. 1993, ApJ, 84, 109
Lefa, E., Rieger, F. M., & Aharonian, F. 2011, ApJL, 740, L64
Mannheim, K., & Biermann, P. L. 1992, A&A, 253L, 21M
Maraschi, L., Ghisellini, G., & Celotti, A. 1992, ApJL, 397, L5
Mattox, J. R., Bertsch, D. L., Chiang, J., et al. 1996, ApJ, 461, 396
Mazin, D., & Goebel, F. 2007, ApJL, 655, L13
Miller, J. S., French, H. B., & Hawley, S. A. 1978, in Proc. of Pittsburgh Conf. on BL Lac Objects, ed. A. M. Wolfe (Pittsburgh, PA: Univ. Pittsburgh)
Murase, K., Dermer, C. D., Takami, H., & Migliori, G. 2012, ApJ, 749, 63M
Nolan, P. L., Abdo, A. A., Ackermann, M., et al. 2012, ApJS, 199, 31
Poutanen, J., & Stern, B. 2010, ApJL, 717, L118
Prandini, E., Mariotti, M., & Tavecchio, F. 2011, Proc. 3rd Fermi Symp., Rome, Italy, eConf C110509
Pühlhofer, G., Bolz, O., Götting, N., et al. 2003, APh, 20, 267
Punch, M., Akerlof, C. W., Cawley, M. F., et al. 1992, Natur, 358, 477
Roustazadeh, P., & Böttcher, M. 2011, ApJ, 728, 134
Roustazadeh, P., & Böttcher, M. 2012, ApJ, 750, 26
Tagliaferri, G., Foschini, L., Ghisellini, G., et al. 2008, ApJ, 679, 1029
Thompson, J. D., Bertsch, D. L., Fichtel, C. E., et al. 1993, ApJS, 86, 629
Urry, C. M., & Padovani, P. 1995, PASP, 107, 803
Vaughan, S., Edelson, R., Warwick, R. S., & Uttley, P. 2003, MNRAS, 345, 1271
Wagner, R. M. 2008, MNRAS, 385, 119
Weekes, T. C., Acciari, V. A., Arlen, T., et al. 2010, IJMPD, 19, 1003
Zhang, J., Liang, E.-W., Zhang, S.-N., et al. 2012, ApJ, 752, 157